Remote Sensing of Environment 167 (2015) 152–167

Contents lists available at ScienceDirect

Remote Sensing of Environment

journal homepage: www.elsevier.com/locate/rse

Relationships between dominant plant species, fractional cover and Land Surface Temperature in a Mediterranean ecosystem

Dar A. Roberts [a,*], Philip E. Dennison [b], Keely L. Roth [c], Kenneth Dudley [b], Glynn Hulley [d]

[a] Department of Geography, University of California Santa Barbara, CA 93106, United States
[b] Department of Geography, University of Utah, Salt Lake City, UT 84112, United States
[c] Department of Land, Air, Water Resources, University of California, Davis, Davis, CA 95616, United States
[d] Jet Propulsion Laboratory, California Institute of Technology, Pasadena, CA 91109, United States

ARTICLE INFO

Article history:
Received 11 June 2014
Received in revised form 4 January 2015
Accepted 16 January 2015
Available online 18 February 2015

Keywords:
HyspIRI
AVIRIS
MASTER
Mediterranean ecosystems
Multiple Endmember Spectral Mixture Analysis
Classification
Land Surface Temperature
Spectroscopy

ABSTRACT

The Hyperspectral Infrared Imager (HyspIRI) is a proposed satellite mission that combines a 60 m spatial resolution Visible-Shortwave Infrared (VSWIR) imaging spectrometer and a 60 m multispectral thermal infrared (TIR) scanner. HyspIRI would combine the established capability of a VSWIR sensor to discriminate plant species and estimate accurate cover fractions with improved Land Surface Temperatures (LST) retrieved from the TIR sensor. We evaluate potential synergies between Airborne Visible/Infrared Imaging Spectrometer (AVIRIS) maps of dominant plant species and mixed species assemblages, fractional cover, and MODIS/ASTER Airborne Simulator (MASTER) LST utilizing multiple flight lines acquired in July 2011 in the Santa Barbara, California area. Species composition and green vegetation (GV), non-photosynthetic vegetation (NPV), impervious, and soil cover fractions were mapped using Multiple Endmember Spectral Mixture Analysis with a spectral library derived from 7.5 m imagery. Temperature-Emissivity Separation (TES) was accomplished using the MASTER TES algorithm. Pixel-based accuracy exceeded 50% for 23 species and land cover classes and approached 75% based on pixel majority in reference polygons. An inverse relationship was observed between GV fractions and LST. This relationship varied by dominant plant species/vegetation class, generating unique LST–GV clusters. We hypothesize clustering is a product of environmental controls on species distributions, such as slope, aspect, and elevation as well as species-level differences in canopy structure, rooting depth, water use efficiency, and available soil moisture, suggesting that relationships between LST and plant species will vary seasonally. The potential of HyspIRI as a means of providing these seasonal relationships is discussed.

1. Introduction

The Hyperspectral Infrared Imager (HyspIRI) has the potential to reduce uncertainties in land–energy–atmosphere interactions and improve our knowledge of ecological effects of climate change. Much of the climate-relevant potential of HyspIRI is derived from independent analysis of the reflected solar spectrum (Visible-Near-Infrared/Short-Wave Infrared, or VSWIR) or the emitted spectrum (Thermal Infrared, or TIR). Examples include improved VSWIR estimates of biophysical properties such as surface albedo, leaf area index (LAI: Asner, 1998; Roberts et al., 2004; Schlerf & Atzburger, 2006), Leaf Mass per Area (LMA: Asner et al., 2011; Serbin, Singh, McNeil, Kingdon, & Townsend, 2014), and fractional cover (Roberts, Smith, & Adams, 1993) and important physiological/biochemical properties such as canopy moisture (Sims & Gamon, 2003; Ustin et al., 1998), light use efficiency (LUE: Gamon, Penuelas, & Field, 1992), nitrogen (Asner & Vitousek, 2005; Martin, Plourde, Ollinger, Smith, & McNeil, 2008; Ollinger, Richardson, Martin, Hollinger, & Frolking, 2008; Townsend, Foster, Chastain, & Currie, 2003), lignin–cellulose (Kokaly & Clark, 1999; Serbin et al., 2014), chlorophyll (Asner, Martin, & Suhaili, 2012; Ustin et al., 2009), or photosynthetic capacity (Serbin, Dillaway, Kruger, & Townsend, 2012). The TIR is critical for quantifying canopy temperature, a fundamental control on rates of photosynthesis, respiration, and transpiration (Gates, 1980) as well as a means for partitioning surface energy balance into latent and sensible heat components, critical elements of the hydrological cycle (Anderson et al., 2011, 2008). Broad measures of canopy greenness combined with air and leaf temperatures, provide measures of plant water stress (Moran, Clarke, Inoue, & Vida, 1994). Because photosynthetic capacity is temperature modulated, VSWIR-derived measures of photosynthetic capacity combined with TIR leaf temperatures offer a mechanistic means toward estimating carbon uptake (Serbin et al., 2012).

Ecosystem composition is an important factor for determining ecosystem response to disturbance and climate change (Schimel et al., 2015). Plant species have a strong impact on biogeochemical cycles (Asner & Vitousek, 2005; Ollinger & Smith, 2005), photosynthetic rates (Robakowski, Li, & Reich, 2012), LMA (Asner et al., 2011), and water use efficiency (McCarthy, Pataki, & Jenerette, 2011; Scherrer,

* Corresponding author. Tel.: +1 805 880 2531; fax: +1 805 893 3146.
E-mail address: dar@geog.ucsb.edu (D.A. Roberts).

http://dx.doi.org/10.1016/j.rse.2015.01.026
0034-4257/

Bader, & Korner, 2011). The combination of leaf-level differences in biochemistry, anatomy, and canopy-level differences in plant architecture and their impacts on scattered, reflected, and emitted radiation have enabled plant species to be discriminated spectrally in the VSWIR (Baldeck et al., 2013; Castro-Esau, Sanchez-Azofeifa, Rivard, Wright, & Quesada, 2006; Clark, Roberts, & Clark, 2005; Dennison & Roberts, 2003a; Feret & Asner, 2011; Goodenough et al., 2003; Youngentob et al., 2011) and TIR (da Luz & Crowley, 2007; Ullah, Schlerf, Skidmore, & Hecker, 2012). Furthermore, plant species have been shown to have distinct canopy temperatures, in part due to differences in water use, and in part due to differences in plant architecture (Leuzinger & Korner, 2007; Leuzinger, Vogt, & Korner, 2010). Topographic factors, such as slope and aspect, can have a strong impact on plant distributions, but would also be expected to impact temperature through radiation balance.

Few studies have combined the power of VSWIR imaging spectrometry and TIR remote sensing to explore species-level relationships. In this paper, we use paired Airborne Visible/Infrared Imaging Spectrometer (AVIRIS) and MODIS-ASTER Airborne Simulator (MASTER) data to evaluate the relationship between plant species/vegetation class, fractional cover, and Land Surface Temperature (LST). The study was conducted in the area surrounding Santa Barbara, California, USA consisting of a mixture of natural vegetation, agriculture, and urbanized areas, using data acquired on July 19, 2011. Plant species and vegetation classes were mapped using Multiple Endmember Spectral Mixture (MESMA: Roberts et al., 1998), which was also used to generate cover fractions for non-photosynthetic vegetation (NPV), green vegetation (GV), soil, impervious surface, and shade. Relationships between the GV fraction and LST as it varied with plant species were evaluated.

2. Methods

2.1. Study site

The study was conducted in the Santa Barbara area, including three 49-km-long east–west flight lines extending from the coast to the crest of the Santa Ynez range (Fig. 1, Runs 20 to 22). A fourth, 43-km-long north–south flight line (Run 19) was also analyzed, and overlapped with the western edge of the east–west lines. All flightlines were acquired on July 19, 2011.

The study area has a Mediterranean climate, characterized by cool winters, warm summers, winter precipitation, and summer drought. Elevation ranges from sea level to a height of 1310 m along the crest of the Santa Ynez Mountains, dropping to 220 m in the interior Santa Ynez Valley. The east–west orientation of the mountains, cold currents along the coast and general pattern of winter storms create a highly contrasting environment with moderate temperatures along the coast, higher temperature extremes in the interior, and high spatial variation in precipitation including significant orographic enhancement on the south facing side of the Santa Ynez Range and a modest rain shadow in the interior. For example, based on a pair of weather stations deployed by UCSB (Roberts, Bradley, Roth, Eckmann, & Still, 2010), the interior station recorded an average annual precipitation of 337 mm from 2007 to 2013, while the coastal station recorded 445.5 mm. 2011 was the wettest year in this time period, with the coastal station receiving 651 mm.

These strong environmental gradients result in significant diversity in vegetation over a relatively short distance. Progressing along Run 19 from north to south (Fig. 1), the interior is dominated by a mixture of open grasslands, oak savannas, open pine forest, and shrublands. Common species include evergreen needle leaf shrubs such as chamise (*Adenostoma fasciculatum*), evergreen and deciduous shrubs such as purple sage (*Salvia leucophylla*), California sage brush (*Artemisia californica*), coyote brush (*Bacharis pilularis*) and California buckwheat (*Eriogonum fasciculatum*), and broadleaf and needle leaf trees including coast live oak (*Quercus agrifolia*), blue oak (*Q. douglasii*), valley oak (*Q. lobata*) and gray pine (*Pinus sabiniana*). Introduced European grasslands are dominated by a mixture of introduced grass and herbaceous species, some natives and large stands of invasive black mustard (*Brassica nigra*). Moving south, the valley floor is dominated by agriculture, including annual and perennial crops (vineyards), bare soil, and a few small urban centers. Highest elevations along the Santa Ynez range are dominated by a mixture of evergreen needle leaf (chamise) and broadleaf shrubs, including several species of Ceanothus (*Ceanothus*

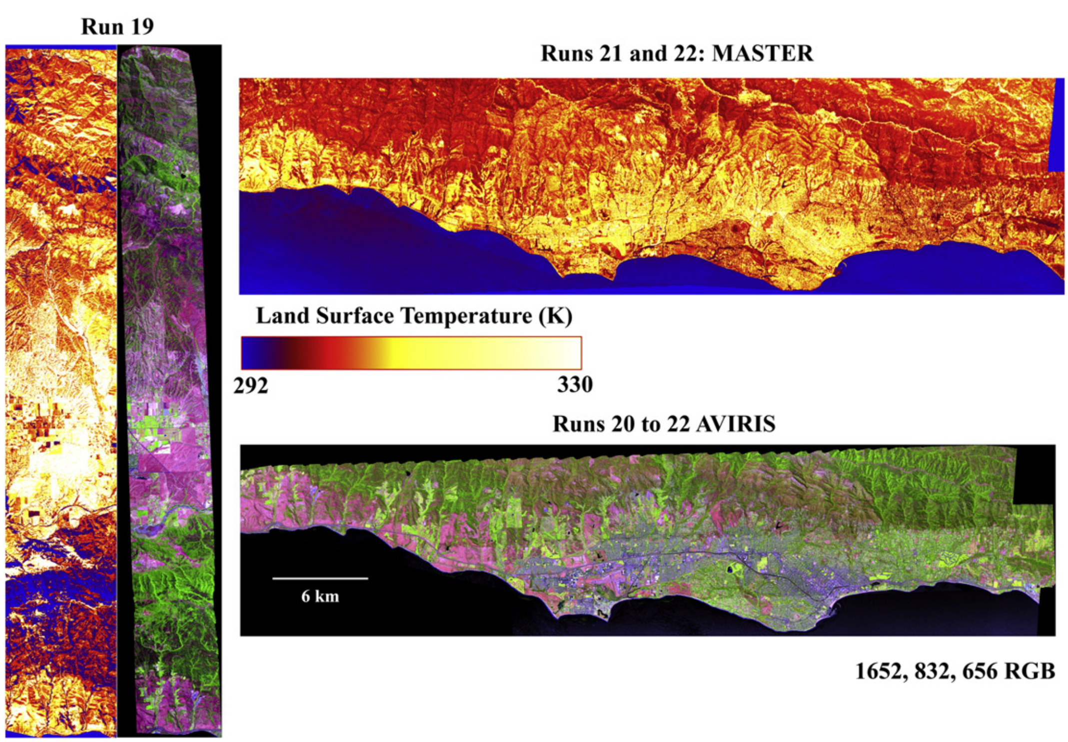

Fig. 1. Study site showing AVIRIS reflectance in three bands (indicated wavelengths are in nm) and MASTER LST for Runs 19 to 22.

megacarpus, *C. spinosus* and *C. cuneatus*), and manzanitas (*Arctostaphylos glauca* and *glandulosa*), and several tree species including large stands of coast live oak, California bay laurel (*Umbellularia californica*), and sycamore (*Platanus racemosa*) in riparian zones. Abundance for many species depends on local edaphic factors. Chamise and manzanita are more common at higher elevations in more rocky terrain, while *C. spinosus* and *Umbellularia* are more common in mesic sites. Coastal sites are dominated by a mixture of introduced European grasslands and invasive mustards, pockets of small shrubs such as coyote brush and purple sage, and local concentrations of coast live oak and riparian species in small canyons. The coasts are also heavily disturbed, including small localized stands of *Eucalyptus*, extensive orchards of avocado (*Persea americana*), and various citrus species. The east–west flights are similar in nature to the southern half of run 19 (Fig. 1), but also include an extensive urban element.

2.2. Data

2.2.1. AVIRIS

Remotely sensed data used in this study were acquired by AVIRIS and MASTER deployed simultaneously on an ER-2 high altitude platform. AVIRIS is a 224 channel imaging spectrometer that samples radiance between 350 and 2500 nm at an approximately 10 nm interval with a full width half maximum of approximately 10 nm and an instantaneous field of view (IFOV) of 1 milli-radian (Green et al., 1998). The data were flown at an average height of 9 km, resulting in a variable ground instantaneous field of view (GIFOV) between 6.8 (Runs 19 and 22) and 7.7 m (Run 20) depending on peak surface elevation below the sensor. Data were acquired between 21 UTC (Run 19) and 21.83 UTC (Run 22), at a solar zenith that increased from 18.6° for the first flight to 26.9° and a solar azimuth that shifted westward from 224° to 246°.

AVIRIS data were calibrated to radiance and then orthorectified by the Jet Propulsion Laboratory (JPL). Surface reflectance was retrieved using ATCOR-4 (Richter & Schlaepfer, 2002) using a rural atmosphere, an initial input visibility of 25 km, and variable water vapor fit on the 940 nm water vapor band as inputs. ATCOR-4 corrects for directional effects using a digital elevation model (DEM) and uses spectral polishing to reduce high frequency spectral artifacts. A DEM is used to calculate sun-sensor geometry and correct all surfaces to reflectance, ρ_L, using local solar zenith and azimuth and an assumed lambertian surface. Cross scene illumination effects are normalized using a multiplicative factor. Defaults use a correction based on the ratio of the cosine of local solar zenith, B_i to a scene dependent zenith, B_T, with the ratio raised to a power b ($\rho_{cor} = \rho_L * G$, where $G = [\cos(B_i)/\cos(B_T)]^b$, where ρ_{cor} is illumination corrected reflectance). ATCOR-4 empirically adjusts parameters to minimize cross scene effects Radiometric spectral polishing identifies all bare soil pixels in an image, then uses a five band moving window to smooth all bare soil spectra. The average departure between measured and smoothed soil spectra is calculated across the entire image, then applied to all pixels to remove high frequency artifacts, primarily due to incomplete atmospheric correction. Default values for BRDF correction and spectral polishing were used in this study (see ATCOR-4 User Guide, 2012).

After reflectance retrieval, all AVIRIS images were resampled to a common 7.5 m resolution using ground control points derived from a 2010 National Agriculture Imagery Program (NAIP) digital orthophoto (ca083) to improve georegistration. Runs 19, 21 and 22 were warped using Delauney triangulation and nearest neighbor resampling, while Run 20, which was mostly ocean, was warped using a second order polynomial and nearest neighbor resampling. Once classified and processed using spectral mixture analysis, Runs 20 to 22 were mosaicked, giving precedence to the southern lines in all cases to take advantage of a superior backscattering view geometry.

2.2.2. MASTER

MASTER is a 50 channel broad band sensor designed to simulate MODIS and ASTER. In this study we focused exclusively on five thermal bands including MASTER bands centered at 8.6139, 9.0531, 10.616, 11.302, and 12.096 μm. MASTER has a 2.2 milli-radian IFOV and a 85.92 FOV (Hook, Myers, Thome, Fitzgerald, & Kahle, 2001) resulting in an IFOV slightly larger than twice that of AVIRIS and an FOV more than twice as wide. Temperature-Emissivity Separation (TES) was performed using the PyMASTER retrieval algorithm developed by JPL. PyMASTER is based on Python scripts and has been updated to simulate the HyspIRI TIR retrieval and atmospheric correction methods outlined in the Algorithm Theoretical Basis Document (ATBD) available at http://hyspiri.jpl.nasa.gov/documents.

Derivation of surface temperature and emissivity from observed TIR radiance is an undetermined problem, and the constraint used for solving the problem is an empirical relationship that predicts the minimum emissivity (ϵ_{min}) from the observed spectral contrast, or minimum–maximum emissivity difference (MMD) for the set of bands being used (Kealy & Hook, 1993; Matsunaga, 1994). The calibration curve defining this relationship is derived from a subset of spectra of different surface materials (rocks, soils, vegetation, snow, and water) from the ASTER spectral library (Baldridge, Hook, Grove, & Rivera, 2009). The calibration curve appropriate for MASTER window bands used in this study (43, 44, 47–49) is:

$$\epsilon_{min} = 0.9921 - 0.75433 \cdot \text{MMD}^{0.7852} \tag{1}$$

where ϵ_{min} is the minimum emissivity for the five window bands, and MMD is the difference between the minimum and maximum emissivity for those bands. TES requires land leaving radiance as input, which is first estimated in an atmospheric correction module using MODTRAN (Berk et al., 2005) and atmospheric profiles from the National Center for Environmental Prediction (NCEP) (Kalnay, Kanamitsu, & Baker, 1990) in which the atmospheric emission, scattering, and absorption by the Earth's atmospheric constituents are removed from the observation. After atmospheric correction and iterative removal of the reflected downwelling radiance in TES, ϵ_{min} is calculated and the full emissivity spectrum can be recovered from the emissivity band ratios (Gillespie et al., 1998).

The TES algorithm is susceptible to errors in retrieved temperature and emissivity due to residual effects from incomplete atmospheric correction, especially over graybody surfaces (e.g. water, vegetation) (Gustafson, Gillespie, & Yamada, 2006). To minimize these atmospheric correction errors, a Water Vapor Scaling method was developed to improve the accuracy of the output parameters from MODTRAN using an Enhanced Multichannel Water Vapor Dependent (EMC/WVD) split-window algorithm (Hulley, Hughes, & Hook, 2012; Tonooka, 2005). Essentially the surface temperature is first estimated over graybody pixels on the scene using the split-window algorithm and these values are used to scale the atmospheric parameters from MODTRAN (transmittance, path radiance, sky radiance), which are then used to estimate the surface radiance input to the TES algorithm. In this study, atmospheric correction was performed using a user-optimized method in which the maximum surface temperature difference was minimized by iteratively scaling the total ozone and water vapor amount in MODTRAN for pixels over a water body. An optimal solution was found by using an ozone scaling factor of 0.5, 370 ppm CO_2, and 0.8 cm for water vapor. These scaling factors were then used in MODTRAN to calculate the atmospheric parameters, which were used to estimate the surface radiance input to the TES algorithm.

Retrieved temperature, referred to as LST, was resampled to a 15 m spatial grid after orthorectification and rotation using parameters supplied by JPL. A second-stage georectification was performed using the same 2010 NAIP dataset. Delauney triangulation was used with nearest neighbor resampling, but only applied to Runs 19, 21, and 22—given the larger FOV of MASTER compared to AVIRIS, Run 20 was not needed.

Finally, to match spatial resolutions with resampled AVIRIS reflectance data, LST was resampled to 7.5 m spatial resolution using nearest neighbor resampling, meaning each 7.5 m pixel was replicated four times.

2.3. Spectral library development

Polygons used to create training and test spectral libraries were based on field assessment, 1 m orthoimagery, and Google Earth Imagery. Each polygon was required to be at least 75% dominated by a single vegetation class, dominant plant species, or land cover class. Here we use dominant plant species to describe vegetation composed of uniform patches of a single plant species or more open stands composed of a dominant canopy species with an exposed understory or substrate. Examples of single-species vegetation classes include *Q. agrifolia*, *C. megacarpus*, *C. spinosus*, and *B. nigra*. Examples of open canopy species that may include mixtures of understory species or substrate include *Quercus douglasii*, *A. fasciculatum*, *P. americana* and *B. pilularis* at the species level, and *Eucalyptus* sp., and *Citrus* sp. at the generic level. Vegetation class is used to describe mixed vegetation assemblages, composed of two or more species such as *A. californica*–*S. leucophylla* (ARCASALE), irrigated grasslands (IRGR), and Mediterranean Annual Grassland and Forbs (MAGF).

Composition of vegetation canopy cover was estimated using a method adapted from Meentemeyer and Moody (2000) using a high-power spotting scope and/or up-close inspection. Once an area at least 75% dominated by a dominant plant species, vegetation class, or land cover class was determined, a polygon containing the area was outlined on a corresponding 1 m orthoimage. Field polygons were assembled over multiple years from 2003 to 2012, with 35 collected in 2003, 65 in 2009, and over 300 in 2012. Polygons generated in 2012 focused on adding additional species and additional urban, agricultural soil, and agricultural residue polygons. Polygons were also edited to remove areas significantly impacted by the Jesusita Fire, which burned 3530 ha of the Santa Barbara front range in May, 2009. Some vegetation and land cover classes (urban, soil, rock, irrigated grass, Mediterranean annual grass/forb, and agricultural residues) were assessed directly from the orthoimagery. Polygons added in 2012 were identified using Google Earth imagery in combination with the 2009 and 2011 AVIRIS imagery (see Roth, 2014). For this paper, all polygons assembled between 2003 and 2012 were individually assessed to verify that vegetation class, plant species, or land cover class were correct.

A total of 306 polygons were used in this study, sampling 24 dominant plant species/vegetation classes/land cover classes (Table 1). Where the same polygon existed in both flight lines in regions of overlap, the polygon was sampled twice to provide spectra from the same surface at both a forward and backscattering view geometry, providing a total of 361 sampled polygons. Test and training spectral libraries were developed using the approach proposed by Roth, Dennison, and Roberts (2012) in which spectra are selected randomly from each polygon. For large polygons, a maximum of 10 spectra were selected for training, with the remainder set aside for testing. For small polygons, no more than 50% of the polygon was sampled for training. Although balanced representation of each species/vegetation class was sought, the number of training pixels varied considerably depending on the spatial extent of the class and its abundance in the Santa Barbara area. For example, California bay laurel (UMCA) was only represented by four polygons, resulting in 40 training spectra and 480 test spectra (Table 1). By contrast, chamise (ADFA) was represented by 28 polygons, providing 276 training spectra and 4988 test spectra. The mean number of sampled polygons for each class was 15, the mean number of training spectra was 149 and the mean number of test spectra was 3396 (Table 1).

2.4. Spectral mixture analysis

Dominant plant species/vegetation class and fractional cover were mapped using MESMA (Roberts et al., 1998). MESMA is an extension of simple spectra mixture analysis in which the number and types of endmembers (EMs) are allowed to vary on a per-pixel basis. Typical EMs include NPV (e.g. litter, stems and branches, senesced grass), GV, soil, and shade (Roberts et al., 1993), but can be extended to include other surfaces such as ash or impervious surfaces (Roberts, Quattrochi, Hulley, Hook, & Green, 2012). MESMA compares multiple models constructed from combinations of two, three, or four EMs, and selection criteria for the best-fit model typically include Root Mean Square Error (RMSE) and constraints that require fractions to be physically reasonable (e.g. between 0 and 100%). In this study, fraction constraints were set at −5 to 105% to allow for some error in minimum and maximum fraction, and the maximum RMSE allowed for a model to fit a pixel spectrum was set to 2.5% reflectance.

In this study, we implemented MESMA in two ways. First, MESMA was used as a classifier, in which a two-EM model (with one species or class EM and a shade EM) was used to assign a class to a pixel. This is one of the most common applications of MESMA and has been used to map species in chaparral (Dennison & Roberts, 2003a; Roth et al., 2012), Eucalyptus subgenera (Youngentob et al., 2011), wetlands (Li, Ustin, & Lay, 2005), and forest plant functional types (Antonarkis, Munger, & Moorcroft, 2014). MESMA can also be used to estimate fractional cover, in which two, three, and four-EM models are combined to produce a single fraction map. RMSE is calculated for each model, and a threshold is used to select between best-fit two, three, and four-EM models (Powell, Roberts, Dennison, & Hess, 2007). "Complexity" indicates the number of EMs used in the selected model for each pixel and fractional cover is reported as the GV, NPV, soil, impervious, and shade fractions modeled for each pixel. A threshold of 0.7 change in RMSE (reflectance units) was selected empirically to determine whether a two, three, or four-EM model should be assigned to each pixel. Thus, if the best-fit three-EM model improved RMSE more than 0.7 over the best-fit two-EM model, the three-EM model was selected over the two-EM model. An example of the three main MESMA products, complexity, 2-EM class, and fractional cover is shown in Fig. 2.

In order to improve MESMA run times, we used Iterative Endmember Selection (IES, Roth et al., 2012; Schaaf, Dennison, Fryer, Roth, & Roberts, 2011) to reduce the size of EM libraries. IES models a spectral library using the spectra from the library as EMs, and progressively adds or subtracts EMs to decrease classification error as measured by an increase in the kappa coefficient (Congalton, 1991). In this study, the training spectral library consisted of 3578 spectra and IES selected 284 EMs, including at least one representative for each class.

EMs selected by IES from a library may not all perform well when applied to an image. To evaluate EMs selected by IES, two-EM models were applied to all four AVIRIS reflectance images and used to map the 24 species/land cover classes. Each of the 284 models was assessed individually based on several criteria including rarity (models that were rare and mapped less than 500 pixels were discarded), purity (highly mixed spectra were discarded) and the extent to which the EM modeled its class correctly. For example, several *Eucalyptus* (EUSP) and irrigated grass (IRGR) EMs were discarded because they tended to map the wrong class and rarely mapped the correct class. This procedure is typically iterative—removing one poorly-behaved model may result in a different model that was well-behaved becoming a poor performer. In this study, four iterations were used, resulting in a library consisting of 224 EMs. Through this process, half of the IRGR EMs and more than half of the EUSP EMs selected by IES were discarded. The 224-EM library was used to run two-EM models on the reflectance images, generating the final vegetation type classifications.

For fraction modeling, the 224-EM library was further subset to reduce run time and improve fraction accuracy. EMs that are clearly mixed might be suitable for classification (such as a pixel dominated by chamise with some exposed soil), but would not be appropriate as a GV EM. EMs that are nearly identical are redundant, and can also be removed. The general procedure for spectral library development, IES EM selection, spectral library refinement, image classification, further

Table 1
Library sampling. NP reports the number of polygons for each species/vegetation class/land cover class along each flight line or in the training and test libraries. NS reports the number of spectra sampled from the polygons, equal to 10 for large polygons or less than 50% for small polygons. Code reports the acronym used for each class throughout the paper.

		r19		r20		r21		r22		Train		Test
Type	Code	NP	NS	NP	NS	NP	NS	NP	NS	NP	NS	NS
Adenostoma fasciculatum	adfa	2	20			1	10	25	246	28	276	4988
Agricultural residues	agres	16	160							16	160	1592
Artemisia cal/Salvia leucophylla	arcasale	13	130			1	10			14	140	4256
Arctostaphylos glauca/glandulosa	argl	1	10					7	70	8	80	1923
Bacharis pilularis	bapi	1	10	8	76	10	97			19	183	962
Brassica nigra	brni	0	0	5	50	9	90	1	10	15	150	5871
Ceanothus cuneatus	cecu	5	50					1	10	6	60	526
Ceanothus megacarpus	ceme							14	140	14	140	2569
Ceanothus spinosus	cesp	6	60			1	10	3	30	10	100	2402
Citrus species	cisp	2	20			11	106	2	20	15	146	1420
Eriogonum fasciculatum	erfa	8	80							8	80	3180
Eucalyptus species	eusp			7	70	12	120	4	40	23	230	6894
Irrigated grass	irgr			1	10	16	160			17	170	2644
Mediterranean Annual Grass/Forb	magf	3	30	3	30	7	70	7	70	20	200	3188
Marsh	Marsh			8	80	10	100			18	180	8923
Persea americana	peam					18	180	8	80	26	260	7115
Pinus sabiniana	pisa	7	70							7	70	2134
Platanus racemosa	plra	1	10			2	20	5	50	8	80	1640
Quercus agrifolia	quag	1	10			9	90	7	70	17	170	3958
Quercus douglasii	qudo	17	170							17	170	5276
Rock	rock	2	20			3	30	3	30	8	80	607
Soil	soil	11	102	1	5	9	86			21	193	2464
Umbellularia californica	umca	1	10					3	30	4	40	480
Urban	urban			6	60	16	160			22	220	6500
	Totals	97	962	39	381	135	1339	90	896	361	3578	81512
								Min		4	40	480
								Max		28	276	8923
								Mean		15	149.1	3396.3
								Stdev		6.6	64.5	2351.2

spectral library refinement and fraction mapping is shown schematically in Fig. 3.

Through removal of redundant and mixed EMs, a 59-EM spectral library (Fig. 4) was used to calculate fractions of NPV, GV, soil, and impervious surfaces. These 59 EMs were combined in two, three, and four-EM models with a shade EM to model the reflectance images. Thirteen EMs were used for NPV, 22 for GV, 8 for soil, and 16 for impervious (Fig. 4). Based on this approach, one 2-EM model with 59 EMs was run, followed by six 3-EM models and four 4-EM models, representing all possible combinations of NPV, GV, soil, and impervious. For this library, this translates to between 104 (NPV-soil) and 352 (GV-impervious) 3-EM combinations and 1664 (NPV-impervious-soil) to 4576 (NPV-GV-impervious) 4-EM combinations.

2.5. Accuracy assessment and statistical analysis

Two-EM model classification accuracy was assessed at pixel and polygon levels by calculating an error matrix from test spectra selected from polygons. At the pixel level, Producer's accuracy, User accuracy, overall accuracy, and kappa were calculated based on the number test spectra pixels assigned to each class. Polygon-level accuracy was assessed based on dominance—a polygon was considered properly classified if the most abundant class for test spectra in the polygon was correct. Polygon-based accuracy did not include unclassified pixels in this assessment—thus a polygon would be considered correctly classified if the most abundant class was correct, even if a majority of the pixels in the polygon were not classified.

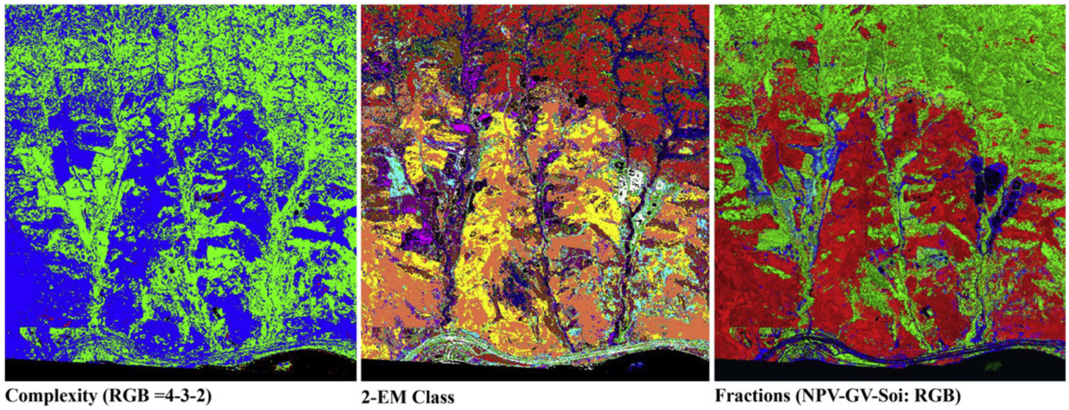

Fig. 2. Complexity (left), Class Assigned from the 2-EM model (center), Fractions of NPV, GV, and soil calculated by fusing mixture models from three levels of complexity.

To evaluate the relationship between fractional cover and LST as it varies across dominant plant species or vegetation class, the average fractional cover and LST for each polygon in the reference set was calculated. GV fraction (y) was plotted against LST (x) and the pattern in GV–LST space was evaluated to determine whether observations were clustered by dominant plant species/vegetation class in the GV–LST space. We used one-way Multivariate Analysis of Variance (MANOVA) to determine if significant differences in GV–LST data existed across classes. MANOVA was run using a Type I sum of squares to account for differences in the number of observations per class. To determine significance between each pair of classes, we also ran pairwise significance tests with the Holm adjustment for multiple comparisons. We also calculated the Bhattacharyya distance (B-dist) between pairs of classes. The Bhattacharyya distance incorporates both the mean and covariance, and it is closely related to classification accuracy via maximum likelihood (Langrebe, 2000). From the B-dist, the upper bounds on misclassification probability can be calculated as $\exp(-b)$; a higher value means two classes are less separable in terms of GV–LST. This analysis was implemented using the 'fpc' package in the R statistical software environment (Hennig, 2014; R Core Team, 2014).

3. Results

3.1. Spectral library

The 59-EM spectral library (Fig. 4) revealed that GV EMs had the highest diversity, requiring 22 spectra to capture the diversity present in the four AVIRIS scenes (Fig. 4b). Anthropogenic vegetated surfaces had the highest reflectance, with the brightest EM being irrigated turf grass (IRGR) from a golf course. The next brightest surfaces were all

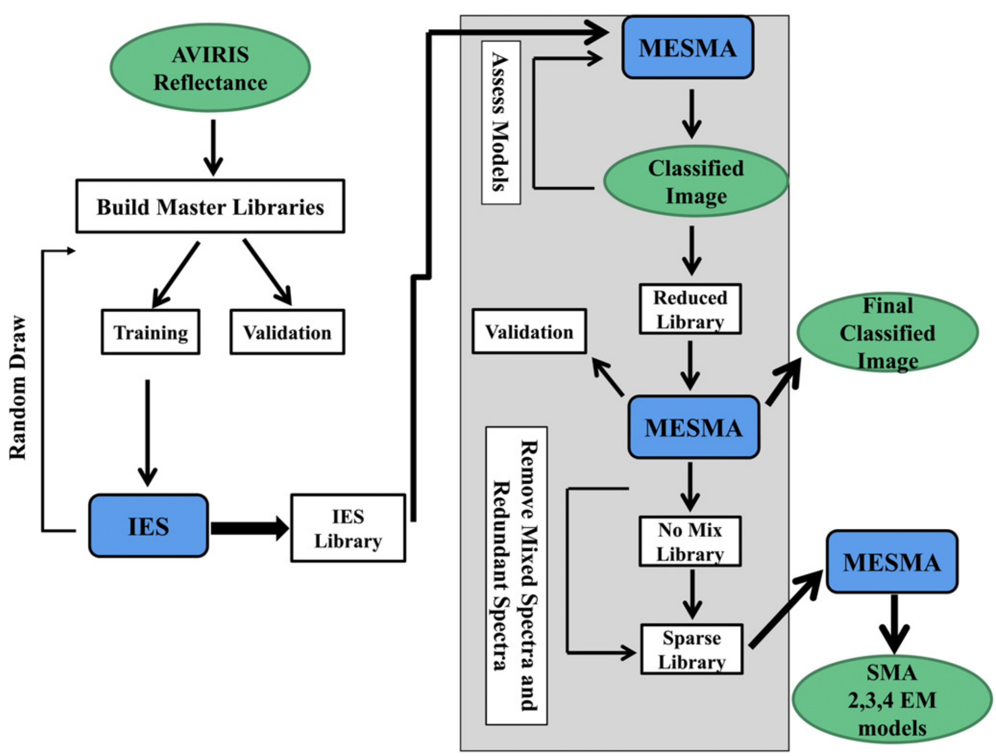

Fig. 3. Schematic showing the general procedure for spectral library development, IES EM selection, spectral library refinement, image classification, further spectral library refinement, and fraction mapping. The left side shows the process of spectral library development from polygons, random sampling, and EM subselection using IES. The right side illustrates the process of generating a classified map using a reduced spectral library, followed by removing all mixed spectra to generate a no-mix library, and further EM subselection to remove redundant spectra and generate the sparse library. Mixed spectra were assessed visually.

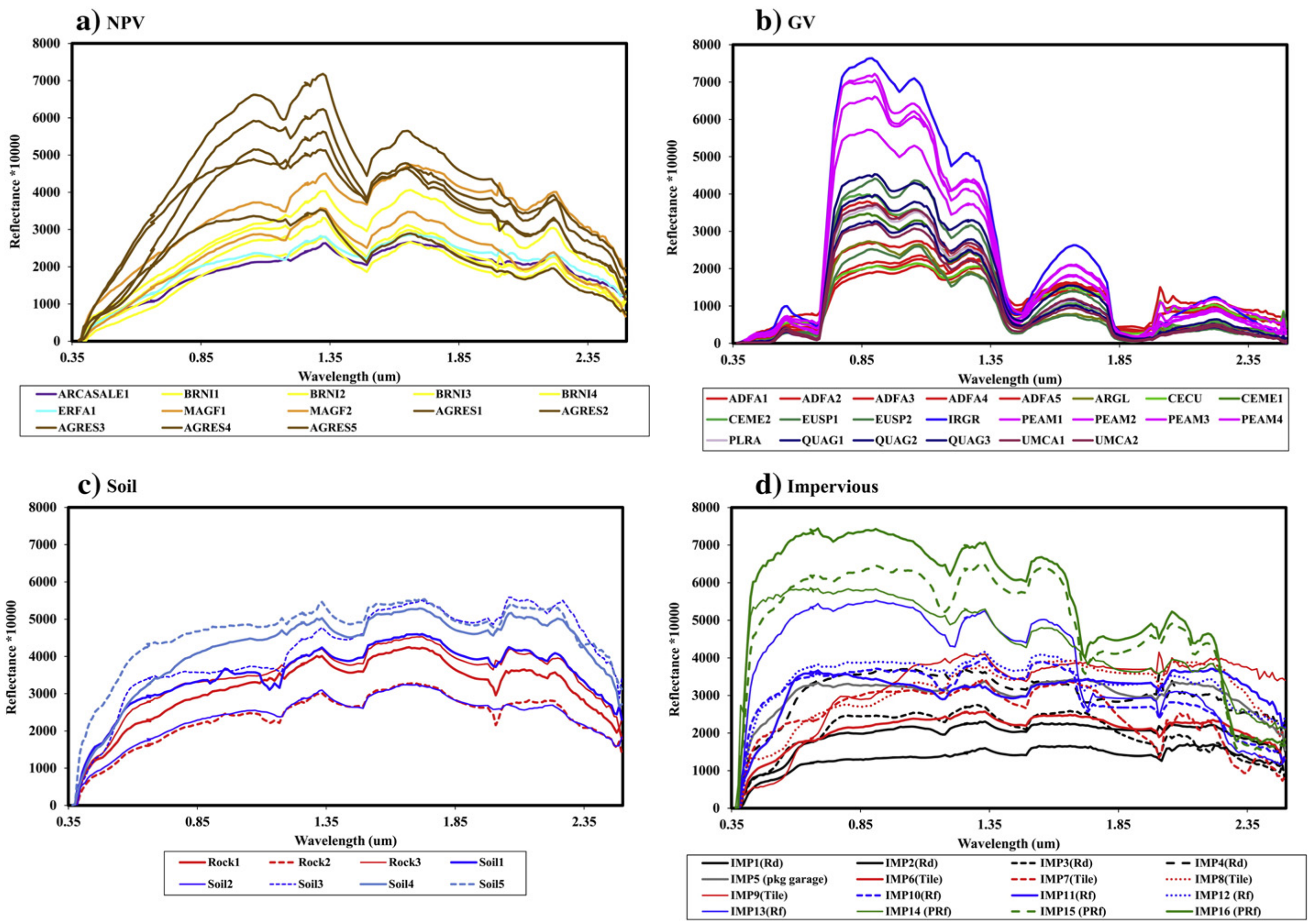

Fig. 4. Spectra of NPV, GV, soil, and impervious EMs from the 59 EM library used for fraction modeling.

orchard spectra of *P. americana* (PEAM). Intermediate reflectance was observed in many of the non-orchard tree species, including *Q. agrifolia* (QUAG), *Eucalyptus* (EUSP), *U. californica* (UMCA), and *P. racemosa* (PLRA). *P. sabiniana* (PISA) was not mapped because of exceptionally low map accuracies (not shown). The lowest reflectance GV spectra were all evergreen shrubs, including five *A. fasculatum* (ADFA), one *Arctostaphlos* (ARGL), one *Ceanothus cuneatus* (CECU), and two *C. megacarpus* (CEME) spectra. Species that were mapped, but proved to not generate a unique endmember spectrum included *Q. douglasii* (QUDO), *Ceanothus spinosus* (CESP), and *B. pilularis* (BAPI).

The second most diverse EM class was urban, consisting of 16 impervious surfaces (Fig. 4d). Using Google Earth Imagery, these materials were specifically identified and included four asphalt road surfaces (IMP01–04), a concrete parking garage (IMP05), four red-tile roofs (IMP06–09), four commercial roofs (IMP10–13), and three roofs coated with oil-based paints (IMP-14–16). These surfaces represented both the highest reflectance (painted roofs) and lowest reflectance (asphalt road) surfaces in the images.

The third most diverse group of EMs was NPV (Fig. 4a). Most of these EMs could be characterized as seasonal NPV, in that most would be live green plants earlier in the spring and treated as GV at that time. One NPV-EM spectrum came from a mixed stand of *A. californica–S. leucophylla* (ARCASALE), four from *B. nigra* (BRNI), one from *E. fasciculatum* (ERFA), two from Mediterranean Annual Grass/Forb (MAGF), and five from agricultural residues (AGRES). All spectra can be characterized as having pronounced lignin–cellulose bands, and little to no evidence of chlorophyll or water absorption features (Fig. 4a). Agricultural residues had the highest reflectance, most likely due to a lack of vertical structure, intermediate reflectance was observed in MAGF and BRNI spectra, and lowest reflectance in the two small shrubs. Eight rock/soil spectra were selected, including three spectra from rock outcrops and five from soils (Fig. 4c). Minor differences in visible reflectance due to iron absorption are apparent, but otherwise soil and rock spectra did not have strong differences in mineral absorption features.

3.2. Classification accuracy

Pixel-based accuracy for the two-EM classified reflectance images was modest, with an overall accuracy of 53.5% and a kappa of 0.510 (Table 2, S1). Producer's and User accuracies varied substantially between classes. The highest accuracies occurred for non-vegetated surfaces including AGRES and SOIL, small shrubs (ERFA, ARCASALE), senesced grasslands (MAGF), URBAN, MARSH, and PEAM, with Producer's accuracies between 60 and 97.8% and User accuracies between 64.2 and 92.1%. High User accuracies ranging from 63.9 to 86.5% were also found for EUSP, BRNI, and QUDO, suggesting that these classes were mapped well where mapped, but were under-mapped overall. Classes that reported relatively high Producer's accuracies included ADFA (72.5%) and QUAG (62.5%), both of which were over-mapped at the expense of other evergreen shrubs or trees. Intermediate User or Producer's accuracies less than 60% were found for BAPI, CEME, and CECU; while PLRA, IRGR, ROCK, and UMCA had very low accuracies. PISA proved so poor it was removed from all modeling efforts. Citrus species (CISP) had a moderately high Producer's accuracy of 52.3%, but low User accuracy due to extensive over-mapping.

Table 2
Producer's/user accuracies at pixel and polygon levels. 6860 pixels of 81,512 test pixels were not classified, equal to 8.4% of the test data set.

Class	Pixel-based			Polygon-based		
	N-pixels	Producer's	User	N-polys	Producer's	User
ADFA	4988	0.725	0.415	27	0.926	0.625
ARCA-SALE	4256	0.860	0.834	14	0.929	0.929
ARGL	1923	0.319	0.444	8	0.375	0.750
BAPI	962	0.589	0.115	12	0.833	0.455
BRNI	5871	0.558	0.757	11	0.636	0.500
CECU	526	0.447	0.390	6	0.667	1.000
CEME	2569	0.556	0.354	14	1.000	0.778
CESP	2402	0.054	0.127	10	0.000	0.000
CISP	1420	0.523	0.194	13	0.923	0.800
ERFA	3180	0.827	0.776	8	0.875	0.778
EUSP	6894	0.285	0.865	15	0.333	1.000
IRGR	2644	0.124	0.232	16	0.750	1.000
MAGF	3188	0.832	0.642	15	0.933	0.700
MARSH	8923	0.604	0.921	11	1.000	1.000
PEAM	7115	0.600	0.890	20	0.900	0.947
PLRA	1640	0.005	0.027	6	0.000	0.000
QUAG	3958	0.625	0.392	14	1.000	0.400
QUDO	5276	0.306	0.639	17	0.294	1.000
ROCK	607	0.112	0.083	6	0.500	1.000
SOIL	2464	0.716	0.728	20	1.000	0.909
UMCA	480	0.121	0.276	4	0.000	0.000
AGRES	1592	0.978	0.875	16	1.000	0.941
URBAN	6500	0.693	0.867	16	1.000	0.941
Overall		0.535			0.748	
Kappa		0.5098			0.734	

A significant contributor to lower pixel-based accuracies was unclassified pixels, totaling 6860 pixels or 8.4% of the test library (Table S1). Unclassified pixels were particularly common in orchards, where trees are found in rows separated by soil or litter, and for BRNI, IRGR, and PLRA. Large numbers of unclassified IRGR pixels, representing 78% of the test data set, were a product of removing half of the IRGR spectra selected by IES. However, we found this was necessary to reduce significant overmapping by some IRGR spectra, which tended to model sunlit parts of tree canopies. Low PLRA accuracies may be a product of insufficient sampling due to a low number of polygons available to IES. PISA, which was excluded as an EM, consisted of 2134 test pixels, and thus also contributed to a general decrease in pixel level accuracy. Removing PISA as a class would have raised overall accuracy 2.6%.

Polygon-level accuracy was substantially higher for most classes (Table 2, Table S2). Polygon-level accuracy was 74.8%, with a kappa of 0.734. Eleven classes had polygon-level Producer's and User accuracies exceeding 70% including ARCA-SALE, CEME, CISP, ERFA, IRGR, MAGF, MARSH, PEAM, SOIL, AGRES, and URBAN. Increases were most pronounced in those classes that had large numbers of unclassified pixels, including CISP, PEAM, and IRGR. Polygon-based accuracies also improved for most evergreen shrubs, including ADFA, ARGL, and CECU. Several classes were never mapped correctly at a polygon level, including CESP, PLRA, and UMCA. Others, including ADFA and QUAG, had very high Producer's accuracies but modest User accuracies. ROCK had a high User accuracy, but modest Producer's accuracy because several reference polygons were misclassified.

Two-EM models were used to generate species/cover maps for all four AVIRIS flight lines (Figs. 5 and 6). The vegetation type map for Run 19 is highly accurate for most of the dominant species and classes (Fig. 5). High accuracies are particularly evident for the small shrubs (ARCASALE, ERFA), senesced grasslands (MAGF, BRNI), agricultural soils and plant residues, QUAG, and ADFA. For example, the northern valley in Run 19 is dominated by a mixture of drought deciduous shrubs, senesced grasslands (MAGF and BRNI), agricultural activities, and oak savannas and forest. Of these, only the oak savannas appear to be poorly mapped. The more mountainous southern part of the flight line is dominated by coast live oak and chamise, and these are the two most prominent species mapped in these locations. The southern segment includes introduced senesced grasslands (MAGF and BRNI), orchards, and *B. pilularis* (BAPI), and these are all mapped as most abundant in this portion of the flight. Poorly mapped species (Table 2, Table S1) are relatively rare so the map errors are not obvious.

An east–west mosaic (Fig. 6), also correctly maps the dominant plant species/vegetation classes in the study area, correctly showing the two most abundant evergreen shrub species (ADFA, CEME), coast live oak (QUAG) dominated slopes and riparian zones, BRNI and MAGF along the coast, MARSH near the airport, orchards (PEAM and CISP) along the foothills, and highly urbanized areas along the coast in the center of the mosaic. Map errors in relatively rare species are not obvious, especially in riparian areas (PLRA and UMCA), mainly because these are not abundant in the study area. Several classes, however, do stand out as having been significantly over-mapped. These include BAPI, which is prominently mapped in recent fire scars, CISP, which is also over-mapped and present in fire scars, and ERFA, which is mapped as abundant in areas known to be rock outcrops. Another significant error is glint off of water surfaces, which is mapped as URBAN due to glint having a relatively flat spectrum similar to some roof materials.

3.3. Cover fractions and temperature

Insets are shown for Run 19 (Fig. 7) and Runs 20–22 (Figs. 8 & 9) showing spectral fractions for NPV, GV, soil, and/or impervious compared to LST derived from MASTER. Along Run 19 two areas are contrasted: a relatively warm, sparsely vegetated region dominated by senesced grasslands and small shrubs (Fig. 7a & c) and an area of densely vegetated shrublands and forests dominated by a high GV fraction and lower LST (Fig. 7b & d). In the more open shrublands, the lowest temperatures occur in areas with the highest GV fractions, dominated primarily by QUDO and QUAG (Fig. 5). The highest temperatures occur in more open areas with a high soil fraction or areas dominated by agricultural residues. Small shrubs have intermediate temperatures around 305 K in areas modeled as mostly consisting of GV.

An example of an urban area is shown in Fig. 8. This is an area dominated by impervious surfaces, MAGF, BRNI, MARSH, orchards (PEAM and CISP), and localized stands of EUSP. High temperatures of up to 330 K occur in areas with a high impervious fraction (Fig. 8a) or high NPV fraction. Intermediate temperatures are observed in orchards, and lowest temperatures in MARSH and *Eucalyptus* stands. A high GV fraction and intermediate temperature is also observed for IRGR, which is left unclassified in Fig. 8c.

Relatively low temperatures were observed in shrub-dominated and riparian dominated areas along the south-facing slope of the Santa Ynez range (Fig. 9). Temperatures in this area were generally low, below 305 K, with highest temperatures localized in riparian areas dominated by QUAG. Contrary to the urban area and central valley, areas with a high soil fraction also tended to have low LST. A lack of correlation between plant species and cover fractions is evident, in which high GV fraction is modeled relatively uniformly throughout most of the eastern half of the image, in an area that shows large, distinct stands of ADFA, CEME, and QUAG. Lower temperatures in the western half correspond to areas that were recently burned in the 2009 Jesusita fire.

3.4. Species, cover fractions and LST

To evaluate the relationships between the GV fraction, LST, and vegetation type, we plotted the mean GV fraction against mean LST for the 306 reference polygons, color coding each polygon to correspond to its vegetation type (color) and plant functional type (symbol). A pronounced inverse relationship was observed between the GV fraction and LST (Fig. 10). Areas with the highest GV fraction also had the lowest temperatures, and areas with low GV fraction, high temperatures. However, significant clustering in the GV–LST space was also observed, with high GV, low LST commonly found for trees, high GV, higher LST found for evergreen shrubs, intermediate GV and higher LST for small shrubs,

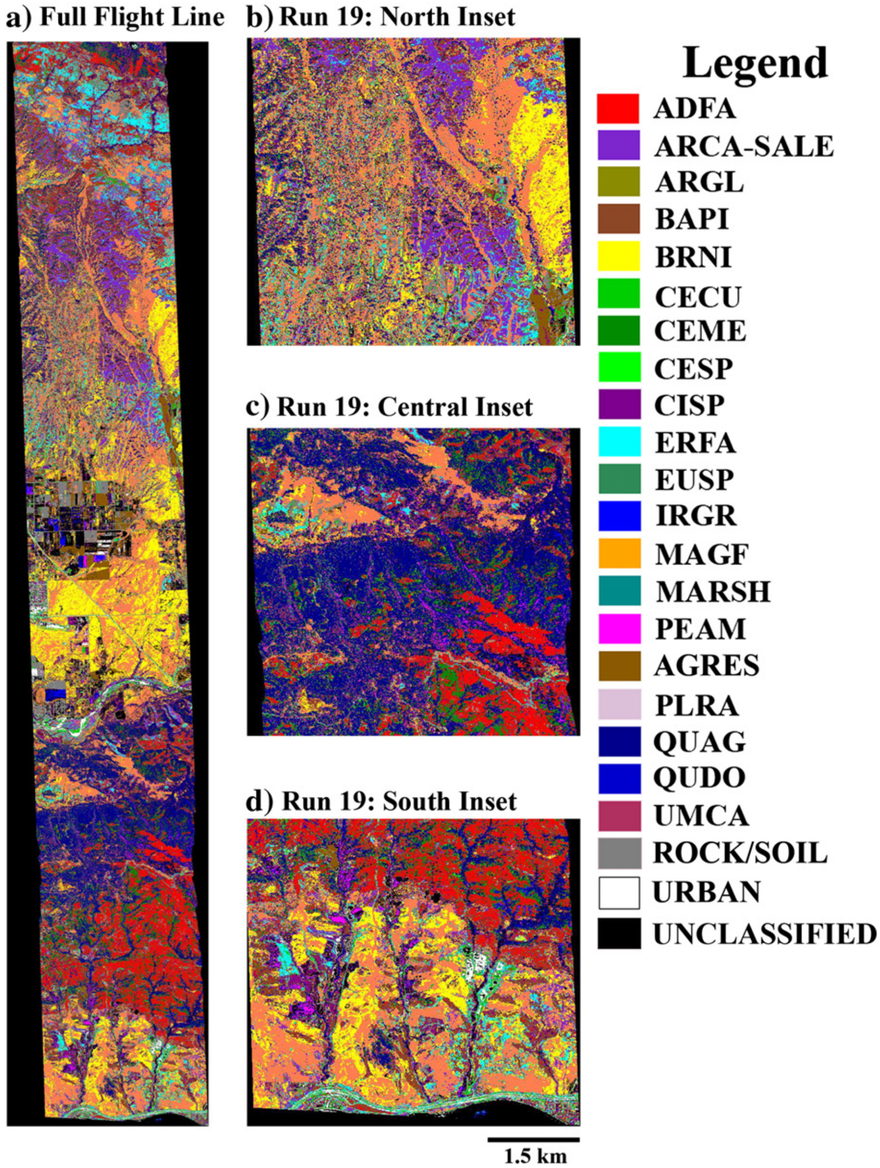

Fig. 5. Classified map of Run 19. Acronyms in the legend are defined in Table 1.

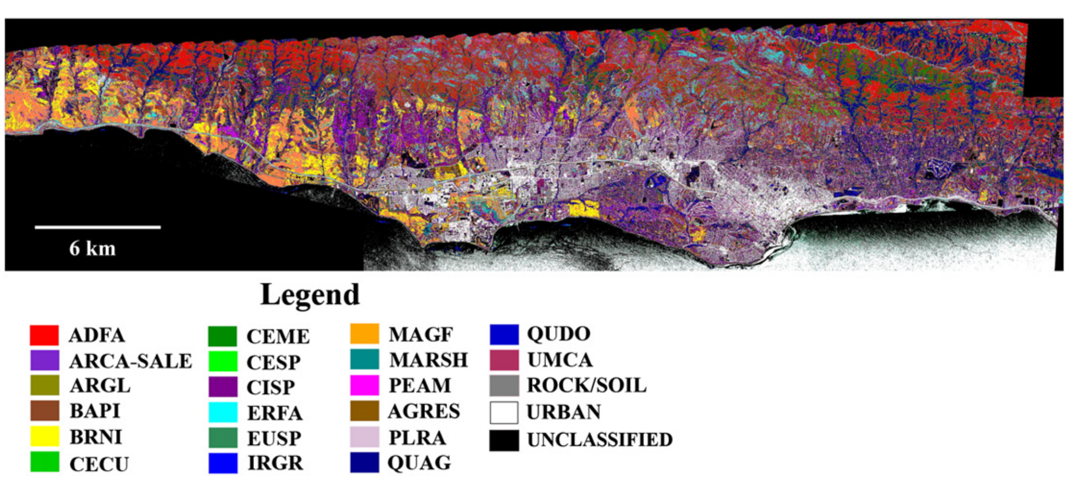

Fig. 6. Classified map of Runs 20 to 22. Acronyms in the legend are defined in Table 1.

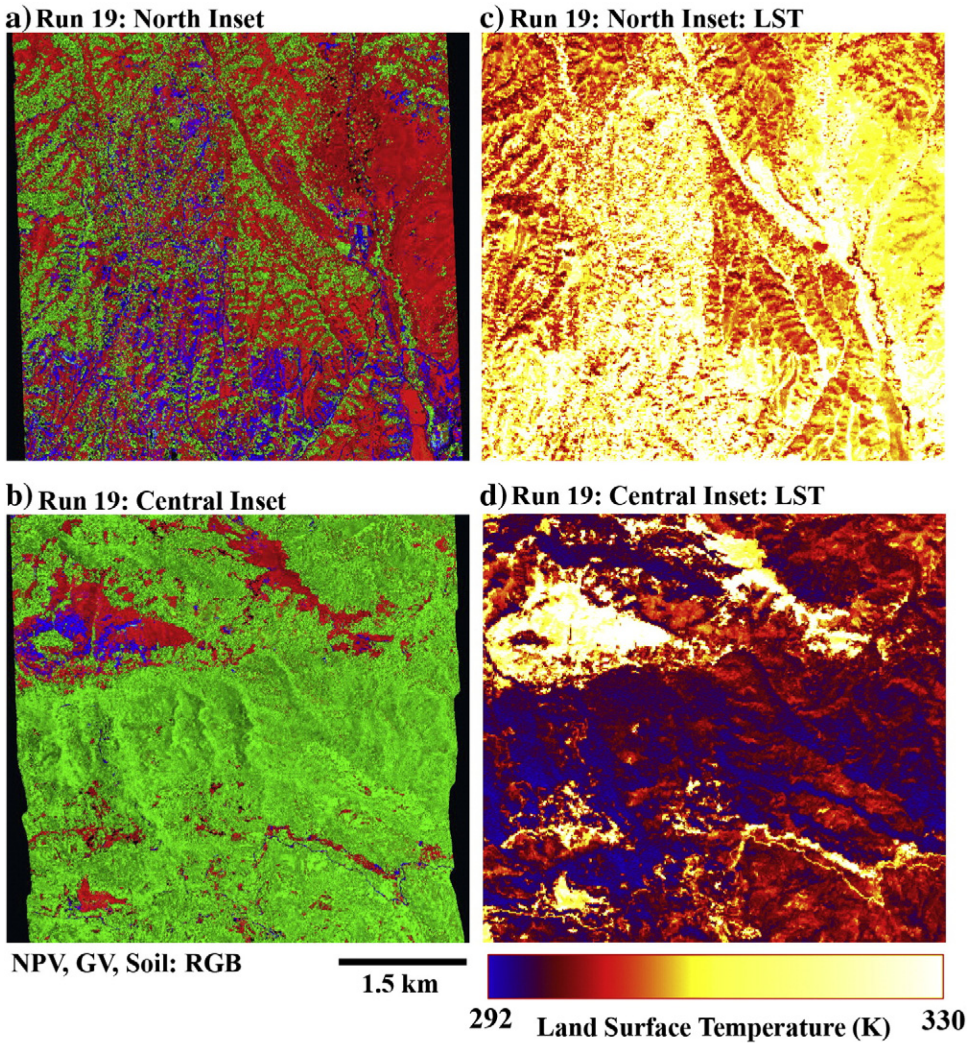

Fig. 7. Fractions of NPV, GV, and soil (a & b), and associated LST (c & d).

and lowest GV, highest LST in MAGF and BRNI. Clear, distinct clusters are present for many plant species/vegetation types. For example, QUDO is clearly offset from QUAG, with similar GV fractions but LST on the order of 5 K higher. Similarly, ERFA is offset from ARCASALE, in which similar LST is observed in both, but lower GV in ARCASALE. MAGF and BRNI form two unique clusters, with BRNI having a slightly higher GV fraction, but significantly lower LST. Of the two orchards, PEAM can be characterized as having a higher GV fraction but slightly lower LST than CISP. Of the various classes, evergreen shrubs appear the least distinct.

MANOVA indicated that significant differences in mean GV and LST existed across classes ($p < 0.001$). Pairwise comparisons using the B-distance revealed that half of the plant species/vegetation classes were unique in GV–LST space (Table 3). Unique clustering, as defined by an upper-bound in misclassification rates of 15% or less in the GV–LST space was found for AGRES, ARCASALE, BRNI, CISP, ERFA, MAGF, PEAM, QUDO, ROCK, SOIL, and URBAN, which met this criteria for 11 or more class pairings. Species that were not separable from other classes in this space included BAPI, CECU, CESP, and MARSH, which had misclassification rates of 15% or less for 5 to 7 class pairings. Evergreen shrubs tended to not be uniquely clustered in the GV–LST space. For example, the lowest misclassification error for ADFA and another evergreen shrub was with CECU, at 38.4%. The lowest misclassification error rate between the three *Ceanothus* species was between CECU and CEME, at 32.1%. Senesced vegetation was highly separable from non-senesced vegetation, but not unique from URBAN, ROCK, and SOIL, which possessed similar low GV fraction and high LST. Visually separable clusters (Fig. 10) prove also to be statistically separable. For example, the upper bound of misclassification between MAGF and BRNI was less than 6%, less than 9% between QUDO and QUAG, and 2.5% between CISP and PEAM. Riparian and mesic species (QUAG, PLRA, UMCA, CESP) tended to cluster in a similar GV–LST space with the lowest upper bound in misclassification rate found between CESP and UMCA at 51%. EUSP also tended to overlap with many tree species in the GV–LST space with a high upper bound in misclassification rate of 88.2% with QUAG. It should be noted that some of the vegetation and cover classes that were mapped at highest accuracy using MESMA (such as MAGF vs soil) did not form unique clusters in the GV–LST space, and others, which were mapped poorly (such as QUDO and CISP) formed unique GV–LST clusters.

4. Discussion

4.1. Classification

While the dominant plant species and vegetation classes in the area were mapped at accuracies exceeding 70%, several less common species were mapped poorly. In general, lowest accuracies were observed for species with the lowest number of training samples and smallest spatial extent. This was particularly true for species that were relatively rare, commonly found in riparian or mesic sites, including UMCA, PLRA, and

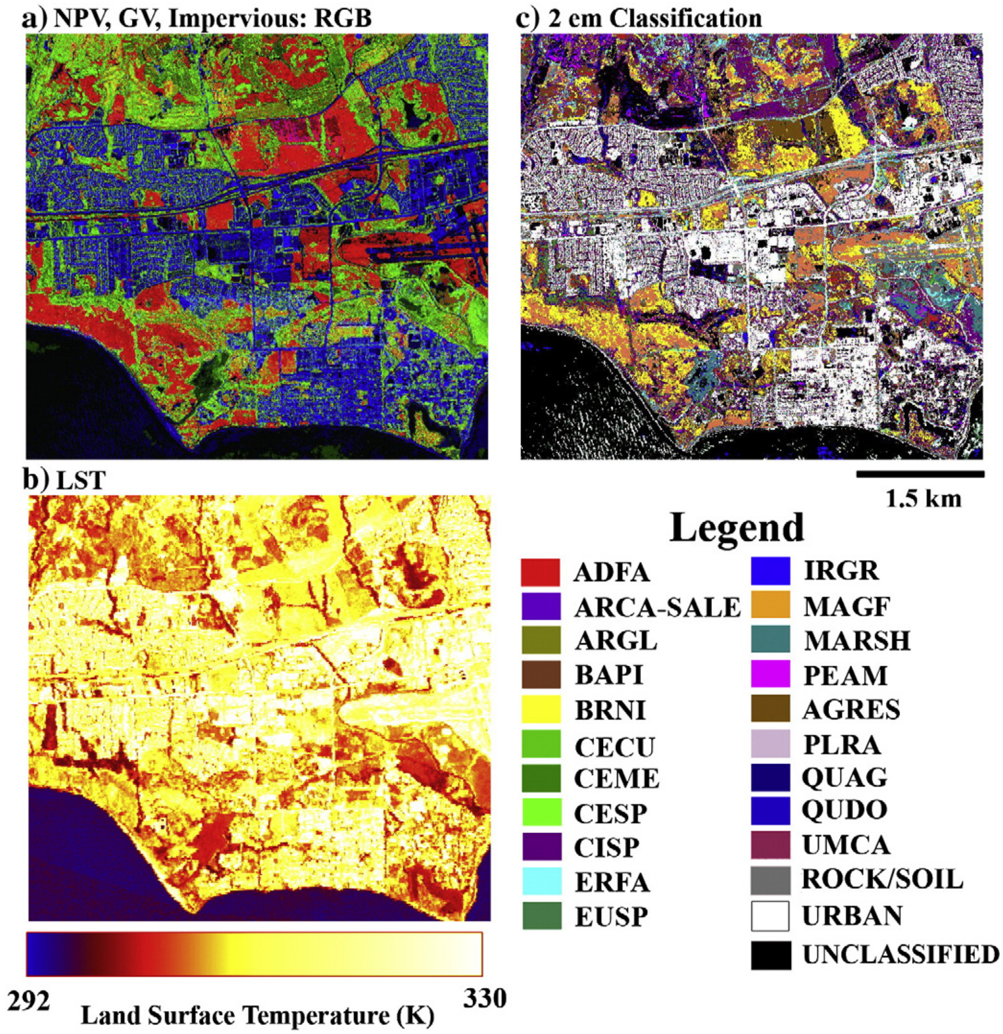

Fig. 8. NPV, GV, impervious (a), LST (b), and two-EM classification (c) for a highly urbanized area centered over Goleta, California. Acronyms in the legend are defined in Table 1.

CESP. The ROCK class was poorly represented in the EM library selected by IES and poorly mapped, suggesting that IES had difficulty identifying unique spectra when training samples were low. One approach to potentially overcome this limitation, proposed by Roth et al. (2012), is the use of multiple random draws, selecting the library that produces the highest kappa out of multiple libraries, in combination with forced EM selection for rare classes. Only a single draw was used in this study, so it is likely that higher accuracies could have been achieved with multiple draws. IES is also not suitable as the only means for identifying a smaller set of spectra required for mapping three or more EMs at higher levels of complexity (i.e., 284 reduced to 59). The approach used here works, but is cumbersome and is one reason why only one random draw was used for IES. One possible strategy would be to use multiple draws and IES to identify the best possible initial library, then to select a smaller subset from that library.

Several other classes proved to be challenging, including BAPI and CISP, which tended to map recent fire scars. We did not include any early successional species in the spectral library and it appears that MESMA drew upon the most similar spectra it could find, which in this case were BAPI and CISP. Additional training data capturing species present in fire scars, and accounting for mixtures of EMs found in fire scars (Kokaly, Rockwell, Haire, & King, 2007), may have improved accuracy.

Another significant source of error was unclassified pixels. Two-EM MESMA classifies a pixel based on the best fit EM in combination with shade. In the event that a pixel is actually a mixture of multiple materials, such as a GV mixed with soil, two-EM MESMA will only model this pixel if the EM library includes an EM that is also mixture of these two materials. In the case of species such as chamise and manzanita, these species are often intermixed with rock and therefore the training library also includes mixed spectra for these classes. As a result, these two classes, in principle, can be mapped accurately. By contrast, a class which is mixed and heterogeneous, where a pixel can be dominated by a single crown, or dominated by substrate between crowns, would likely be poorly mapped using two-EM MESMA because many pixels would require a third EM to be modeled accurately. This was likely the case for orchards, in which large numbers of test pixels for PEAM and CISP went un-modeled. This was also true in urban areas where impervious surfaces are mixed with tree crowns or lawns. Accuracy assessment at the polygon level showed a dramatic increase in accuracy, we suspect, largely due to a reduced impact of unclassified pixels. One alternative, proposed by Franke, Roberts, Halligan, and Menz (2009) is to classify three-EM models (two bright classes and shade) based on the EM that comprises the largest fraction in the pixel. Thus, a pixel composed of CISP, soil, and shade, would be classified as CISP if the GV fraction was highest, or soil if the soil fraction was highest. However, including a larger number of EMs in the library used for mapping fractions to account for all possible species would have greatly increased the number of model combinations for three and four-EM models.

Several other factors should be taken into consideration regarding vegetation type classification. First, accuracy reported here may be over reported due to autocorrelation within polygons used for training

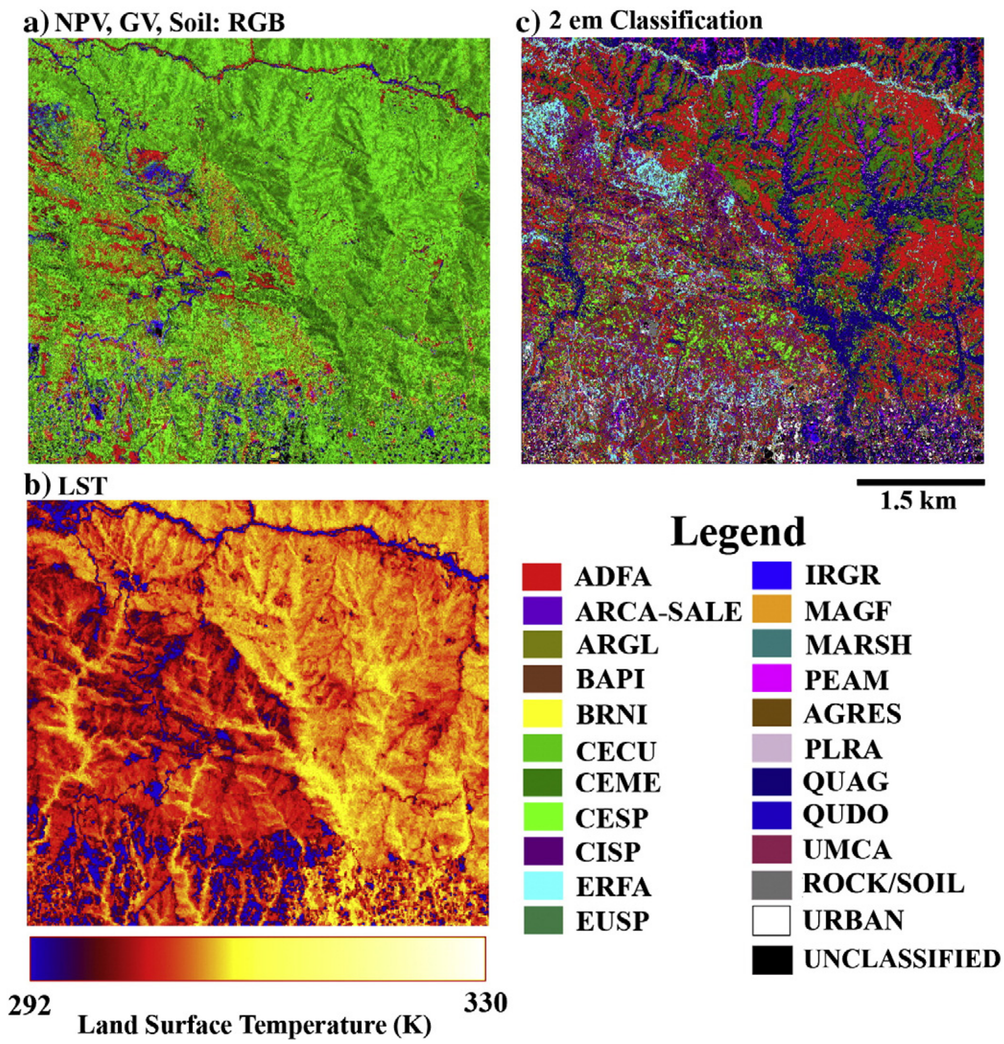

Fig. 9. NPV, GV, and soil (a), LST (b), and two-EM classification (c) for a shrub dominated landscape on the south facing slope of the Santa Ynez Range. Acronyms in the legend are defined in Table 1.

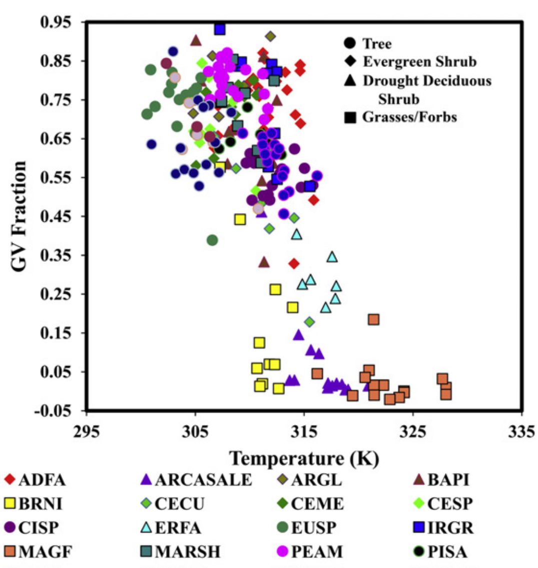

Fig. 10. GV (y) plotted against LST (x). Colors and symbols correspond to different vegetation types. Different symbols are used for each plant functional type, defined in the upper right corner of the figure.

and validation. However, while the training and test data sets were not completely independent, the training spectra subset and the spectra selected by IES were a very small percentage of all polygon spectra. For example, out of 85,090 spectra extracted from polygons, only 3578 spectra (4%) were used for the training subset. Of these 3578 spectra, only 224 were selected by IES, representing a further reduction to 0.2% of the original spectral library. Furthermore, of the original 361 polygons in the image, only 137 unique polygons were represented in the IES library, equal to 37.9% of the training polygons. While autocorrelation within a polygon is present, 62% of the polygons were not sampled by IES.

The research presented here is also based on a single date of imagery, acquired in a relatively wet year in early summer. Dennison and Roberts (2003b) found that seasonality had a significant impact on EM selection and classification accuracy, with highest accuracies found for late spring. Given the high levels of precipitation and cool temperatures in 2011, July 19th may have been more similar to a late spring acquisition than early summer, and thus high levels of accuracy would be expected. Had this analysis used a data set acquired during a drier year or in fall, very different results may have been obtained. The potential of incorporating seasonal imaging spectrometry to map plant species has been largely unexplored. Recent examples, in which seasonal Hyperion was used to improve detection of an invasive tree species on Hawaii, were presented by Somers and Asner (2012, 2013). Roth

Table 3
Upper bound of the misclassification rate based on paired B-distances. Colors indicate misclassification rates below 15% (Green), 15 and 30% (orange), and 30 to 50% (yellow). The table is divided into two halves (a and b) for clarity.

a)

	adfa	agres	arcasale	argl	bapi	Brni	cecu	ceme	cesp	cisp	erfa	eusp
agres	0.000	–	–	–	–	–	–	–	–	–	–	–
arcasale	0.023	0.449	–	–	–	–	–	–	–	–	–	–
argl	0.657	0.000	0.001	–	–	–	–	–	–	–	–	–
bapi	0.795	0.005	0.082	0.683	–	–	–	–	–	–	–	–
brni	0.144	0.061	0.348	0.061	0.284	–	–	–	–	–	–	–
cecu	0.384	0.087	0.338	0.235	0.659	0.337	–	–	–	–	–	–
ceme	0.558	0.000	0.002	0.871	0.682	0.086	0.321	–	–	–	–	–
cesp	0.424	0.000	0.012	0.621	0.786	0.163	0.542	0.737	–	–	–	–
cisp	0.518	0.000	0.020	0.038	0.531	0.152	0.479	0.065	0.229	–	–	–
erfa	0.277	0.156	0.346	0.059	0.325	0.080	0.567	0.062	0.070	0.411	–	–
eusp	0.319	0.000	0.013	0.490	0.681	0.133	0.417	0.550	0.843	0.176	0.059	–
irgr	0.884	0.001	0.019	0.614	0.692	0.062	0.216	0.454	0.228	0.459	0.342	0.172
magf	0.000	0.753	0.428	0.000	0.006	0.053	0.093	0.000	0.000	0.000	0.190	0.000
marsh	0.751	0.042	0.177	0.557	0.860	0.199	0.645	0.515	0.467	0.585	0.570	0.336
peam	0.547	0.000	0.000	0.826	0.582	0.042	0.138	0.695	0.428	0.025	0.069	0.294
pisa	0.668	0.000	0.004	0.288	0.644	0.110	0.380	0.445	0.488	0.521	0.214	0.338
plra	0.281	0.001	0.044	0.336	0.630	0.221	0.589	0.457	0.811	0.274	0.092	0.858
quag	0.316	0.000	0.009	0.523	0.652	0.133	0.377	0.641	0.836	0.136	0.034	0.882
qudo	0.594	0.000	0.009	0.126	0.512	0.069	0.279	0.156	0.172	0.834	0.441	0.129
rock	0.000	0.792	0.434	0.000	0.003	0.065	0.068	0.000	0.000	0.000	0.130	0.000
soil	0.000	0.710	0.327	0.000	0.003	0.082	0.047	0.000	0.000	0.000	0.093	0.000
umca	0.109	0.000	0.008	0.200	0.309	0.077	0.270	0.257	0.510	0.076	0.006	0.510
urban	0.009	0.469	0.560	0.000	0.041	0.245	0.197	0.000	0.002	0.006	0.340	0.004

b)

	irgr	magf	marsh	peam	pisa	plra	quag	qudo	rock	soil	umca	urban
magf	0.002	–	–	–	–	–	–	–	–	–	–	–
marsh	0.788	0.045	–	–	–	–	–	–	–	–	–	–
peam	0.591	0.000	0.580	–	–	–	–	–	–	–	–	–
pisa	0.536	0.000	0.601	0.204	–	–	–	–	–	–	–	–
plra	0.075	0.001	0.279	0.087	0.330	–	–	–	–	–	–	–
quag	0.156	0.000	0.298	0.294	0.342	0.790	–	–	–	–	–	–
qudo	0.612	0.000	0.644	0.146	0.709	0.092	0.088	–	–	–	–	–
rock	0.001	0.691	0.034	0.000	0.000	0.000	0.000	0.000	–	–	–	–
soil	0.001	0.785	0.024	0.000	0.000	0.000	0.000	0.000	0.797	–	–	–
umca	0.011	0.000	0.077	0.031	0.142	0.635	0.438	0.005	0.000	0.000	–	–
urban	0.018	0.751	0.110	0.000	0.001	0.013	0.003	0.005	0.430	0.509	0.001	–

(2014) evaluated the potential of using monthly spectra to discriminate two evergreen shrub species, an annual and perennial grass species, and two small shrubs in the Santa Barbara area, finding that each species pair was statistical significantly different during certain times of the year; yet the timing of best separation varied by species and geographically between inland and coastal sites. The potential of improved species mapping using seasonal information may be explored using recent HyspIRI-like data sets acquired as part of the NASA-funded HyspIRI Preparatory Campaign, in which at least three dates of AVIRIS and MASTER were acquired in 2013 and 2014. The importance of seasonal information for mapping species argues strongly for the value of a mission like HyspIRI, which could provide monthly observations at a fine enough spatial resolution to account for geographic variation.

Other classification techniques could prove superior to MESMA for mapping dominant plant species. For example, Clark et al. (2005) found that Linear Discriminant Analysis (LDA) far outperformed MESMA for discriminating plant species in the tropics while Baldeck et al. (2013) achieved high accuracies using a Support Vector Machine in African savannas. Roth (2014) found that different combinations of training data selection, dimension reduction techniques and classification methods impacted species mapping accuracy in several forested ecosystems, a wetland, and the Mediterranean ecosystem used in this analysis. LDA, Canonical Discriminant Analysis (CDA), and MESMA performed similarly across sites, but frequently LDA and CDA outperformed MESMA. Beyond this, the authors found a significant decrease in accuracy when using IES-selected training data vs. the entire training spectral library. Multiple approaches also exist for identifying EMs, including Vertex Component Analysis (Nascimento & Bioucas-Dias, 2005) as one example. MESMA can be combined with other classifiers to better account for EM variability between classes in the unmixing process.

4.2. Vegetation–LST relationships

Clustering by species was observed between GV fraction and LST, and statistical analysis found significant differences between many pairs of species. Several factors may contribute to plant species occupying a specific niche in GV–LST space. Controls on plant canopy temperatures include topographic factors, such as slope and aspect which controls radiation balance (Dubayah & Rich, 1995), plant architecture and gap fraction (Leuzinger et al., 2010; Scherrer et al., 2011), plant–water relations modifying rates of evapotranspiration (e.g. McCarthy et al., 2011), and canopy optical properties, such as the ratio of lower emissivity stems and litter to higher emissivity leaves. Tree species, such as EUSP, QUAG, and PEAM, tended to plot at high GV, low LST with lowest temperatures observed in the more open EUSP canopies, followed by QUAG, which is distributed more on north and easting facing slopes or riparian zones. QUDO and CISP have shorter statured canopies than EUSP, consisting either of a grass understory (QUDO) or litter/soil background. These had the highest LST and lowest GV of the tree classes, likely due to their shorter stature. Of the evergreen shrub species, CESP, which is distributed in more mesic sites, also had the lowest temperature. Higher LST was observed in most other evergreen shrub species, with highest LST and highly variable GV observed in ADFA, a species that tends to form more open, rocky stands. Comparison of two small-shrub classes, ARCASALE and ERFA, showed some of the most pronounced differences in the GV–LST relationship. In this case, differences reflect the water status of the two plants. ARCASALE tends to have very shallow root systems, very high photosynthetic rates in early spring and senesces by summer during which leaves are either shed, or curled (Eliason & Allen, 1997). By comparison, ERFA has deeper roots and thicker, more drought resistant needle shaped leaves (Kummerow et al., 1977) and thus is able to retain green leaves throughout the summer. Similar, high LST for these two species suggests that neither was actively transpiring. Differences in vertical stature likely impacted GV–LST relations for the forbs and grasses, with vertically-oriented stands of senesced BRNI plotting as much as 10°C cooler than shorter stature MAGF. Overall, higher LST in senesced vegetation illustrates the importance of root zone moisture for maintaining high rates of evapotranspiration and lower canopies temperatures. For example, irrigated grasslands occupy a region of higher GV and lower LST than natural grasslands, in large part because of senescence induced by water stress in annual plants.

An alternate framework can be used to interpret the GV–LST relationships. Moran et al. (1994) proposed a means for assessing crop water stress, in which air–canopy temperature differences are plotted against a measure of greenness from vegetation indices. In this framework, well watered vegetation occupies a region with a high vegetation index while water stressed vegetation has a similarly high index value, but elevated surface–air temperature differences. Based on this framework, EUSP, UMCA, and QUAG would be viewed as least water stressed, evergreen shrubs and orchards more water stressed, and ERFA the highest water stress of the green plants.

This study represents a single snapshot of GV and LST over a relatively limited geographic extent, but GV–LST relationships likely have both temporal and spatial variation. Seasonal and annual variability in precipitation and temperature would be expected to produce greater variation in both GV and LST for shallow-rooted species. For example, MAGF and BRNI were both senesced in the data used for this study. These species occupy a region of low GV and high LST, but would be expected to move significantly in the direction toward higher GV earlier in the season. Shallower rooted species would also be expected to express greater variability in response to longer-term fluctuations in temperature and precipitation. Deeper rooted species such as EUSP or QUAG, which have more reliable access to water (Canadell et al., 1996), may show reduced seasonal variability but still respond to longer-term drought. Species sensitivity to soil water could be monitored by examining changes in GV–LST relationships over time, and predictable changes in these relationships may provide an alternate approach to species mapping (e.g. Nemani & Running, 1997). GV–LST relationships may also be useful for mapping variability in species response to environmental factors across local-to-regional geographic scales. Phenotypic variation and ecotypic differentiation can produce intraspecific differences in response to water stress across gradients in latitude, elevation, and moisture (e.g. Abrams, 1994; Sparks & Black, 1999). HyspIRI-like data could be used to explore intraspecific variations in GV–LST relationships that may occur with slope and aspect or across precipitation and temperature gradients.

4.3. Relationships to HyspIRI

Two major differences exist between the data used in this study and the data that the HyspIRI mission would deliver as currently proposed. The potential of temporal sampling has already been discussed; the 19-day repeat of HyspIRI would be anticipated to provide improved species discrimination through phenology and the ability to monitor seasonal shifts in GV–LST relationships. The other difference is the impact of the proposed 60 m spatial resolution of HyspIRI. Based on prior work, we hypothesize fractions of GV, NPV, soil, and impervious would scale relatively well between the 7.5 m resolution used in this study and the 60 m resolution of HyspIRI. For example, Roberts et al. (2012) evaluated combined VSWIR-TIR synergies at multiple spatial resolutions, including 7.5, 15, and 60 m. At 60 m resolution, classification of the urban environment was not feasible but fractions were portable across all spatial scales, especially for GV and NPV. In past work, comparing MODIS 500 m resolution data to 20 m AVIRIS data, fractions were also portable across scales (Roberts, Dennison, Peterson, Sweeney, & Rechel, 2006).

Classification accuracy for vegetation type may be scale dependent, remaining high for classes that tends to form large patches, but declining for rare or spatially limited classes. For example, Roth (2014) evaluated a range of factors that may impact HyspIRI performance, including the impact of spatial resolution on classification accuracy. Similar to Schaaf et al. (2011), Roth (2014) found that highest classification accuracies were found at coarser spatial resolutions, 40 m for Schaaf et al., and typically 60 m for Roth.

To evaluate the impact of a 60 m spatial resolution on this study, we redid the analysis at 60 m for one flight line (run 19). We aggregated the original 7.5 m AVIRIS to 60 m, and then processed these data to create a vegetation type classification and generate fractions using MESMA. The final results matched our predictions well, with an overall classification agreement of 37% for species/vegetation class/land cover class.

Table 4
Relationship between NPV, GV, soil, and impervious at 7.5 m (x) and 60 m (7).

	NPV	GV	soil	impervious
Slope	1.044	1.067	1.212	0.85
Intercept	−0.02	0.046	−0.009	−0.007
r^2	0.672	0.691	0.549	0.293

Common classes that occur in large patches showed highest agreement (same class at both scales) between 7.5 and 60 m, ranging from a low of 45% (ERFA) to a high of 51.4% (ADFA). Very poor agreement (10% or less) was observed for rare classes that often occur in small patches. Cover fractions, as expected, scaled well from 7.5 to 60 m (Table 4). Highest correlations were observed for NPV and GV, with slopes near 1 for both, intercepts near zero and r^2 values of 0.67 and 0.69, respectively. Relatively modest correlation coefficients are a product of scatter that results from MESMA, in which a 60 m pixel would be modeled by, at most, four endmembers. This same pixel consists of 64 7.5 m pixels, each of which may have a different set of endmembers depending on the homogeneity of the area. A patch significantly larger than 60 m would be expected to produce the same fractions at both scales, yet patches significantly smaller than 60 m could be modeled by as many as 64 unique models compared to one set at 60 m. Lower correlations were observed for soil fraction, which was overestimated at 60 m, and impervious surface fraction, which was underestimated. This is consistent with the high spectral ambiguity between soils and impervious spectra and the fine spatial scale of roads. From this analysis, we conclude that 60 m HyspIRI data would be able to estimate cover fractions accurately, and classify dominant plant species, vegetation classes, and land-cover classes accurately for the more abundant, spatially extensive classes.

5. Conclusions

The HyspIRI mission would provide a unique pairing of a VSWIR imaging spectrometer and TIR broadband sensor, providing global measurement for monitoring of vegetation. In this paper, we used paired AVIRIS and MASTER data to evaluate potential synergies between VSWIR and TIR data. Specifically, we evaluated the relationships between plant species/vegetation classes, cover fractions mapped with AVIRIS, and LST estimated using MASTER at 7.5 m spatial resolution.

A 224-EM library was used with 2-EM MESMA to map plant species and vegetation classes. The resulting map of vegetation type proved to be reasonably accurate, with 53% pixel-level accuracy and 74% polygon-based accuracy. Maps generated using this approach likely had higher accuracies because the largest errors occurred in relatively rare classes, which were proportionally over-represented in the test dataset. Spectral fractions mapped using a 59-EM subset demonstrated a strong inverse relationship between GV fraction and LST, and significant species-level clustering in the GV–LST space. The combination of VSWIR imaging spectrometer and TIR data represents a significant opportunity for understanding dynamic, species-dependent surface reflectance and LST. The potential use of seasonal information, either as a means to improve classification accuracy or as an opportunity to observe how species clusters in the GV–LST space shift seasonally or vary spatially, represents a very important new area for further research. New datasets being acquired by the HyspIRI Preparatory Campaign will allow assessment of seasonal change in GV–LST relationships, but these relationships can only really be fully explored by a mission such as HyspIRI.

Acknowledgments

We wish to thank the Jet Propulsion Laboratory for providing radiometrically calibrated, orthorectified AVIRIS and MASTER data. This research was supported in part by NASA Grants NNX11AE44G, *Evaluation of Synergies between VNIR-SWIR and TIR Imagery in a Mediterranean-climate ecosystem* and NNX12AP08G, *HyspIRI discrimination of plant species and functional types along a strong environmental-temperature gradient*. A portion of this work was carried out at the Jet Propulsion Laboratory/California Institute of Technology, Pasadena, California, under contract with the National Aeronautics and Space Administration.

Appendix A. Supplementary data

Supplementary data to this article can be found online at http://dx.doi.org/10.1016/j.rse.2015.01.026.

References

Abrams, M.D. (1994). Genotypic and phenotypic variation as stress adaptations in temperate tree species: A review of several case studies. *Tree Physiology*, *14*, 833–842.
Anderson, M.C., Kustas, W.P., Norman, J.P., Hain, C.R., Mecikalski, J.R., Shultz, L., et al. (2011). Mapping daily evapotranspiration at field to continental scales using geostationary and polar orbiting satellite imagery. *Hydrology and Earth System Sciences*, *15*, 223–239.
Anderson, M.C., Norman, J.M., Kustas, W.P., Houborg, R., Starks, P.J., & Agam, N. (2008). A thermal-based remote sensing technique for routine mapping of land-surface carbon, water and energy fluxes from field to regional scales. *Remote Sensing of Environment*, *112*, 4227–4241.
Antonarkis, A.S., Munger, J.W., & Moorcroft, P.R. (2014). Imaging spectroscopy- and lidar-derived estimates of canopy composition and structure to improve predictions of forest carbon fluxes and ecosystem dynamics. *Geophysical Research Letters*, 2535–2542. http://dx.doi.org/10.1002/2013GL058373.
Asner, G.P. (1998). Biophysical and biochemical sources of variability in canopy reflectance. *Remote Sensing of Environment*, *64*(3), 234–253.
Asner, G.P., Marten, R.E., Tupayachi, R., Emerson, R., Martinez, P., Sinca, F., et al. (2011). Taxonomy and remote sensing of leaf mass per area (LMA) in humid tropical forests. *Ecological Applications*, *21*(1), 85–98.
Asner, G.P., Martin, R.E., & Suhaili, A.B. (2012). Sources of canopy chemical and spectral diversity in lowland Bornean forest. *Ecosystems*, *15*, 504–517.
Asner, G.P., & Vitousek, P.M. (2005). Remote analysis of biological invasion and biogeochemical change. *Proceedings of the National Academy of Sciences of the United States of America*, *102*(12), 4383–4386.
ATCOR-4 User Guide, Version 6.2 BETA (2012). *Atmospheric/topographic correction for airborne imagery*. (197 pp.).
Baldeck, C.A., Colgan, M.S., Feret, J. -B., Levick, S.R., Martin, R.E., & Asner, G.P. (2013). Landscape-scale variation in plant community composition of an African savanna from airborne species mapping. *Ecological Applications*, *24*(1), 84–93.
Baldridge, A.M., Hook, S.J., Grove, C.I., & Rivera, G. (2009). The ASTER Spectral Library Version 2.0. *Remote Sensing of Environment*, *114*, 711–715.
Berk, A., Anderson, G.P., Acharya, P.K., Bernstein, L.S., Muratov, L., Lee, J., et al. (2005). MODTRAN™ 5, a reformulated atmospheric band model with auxiliary species and practical multiple scattering options: Update. In S.S. Sylvia, & P.E. Lewis (Eds.), *Algorithms and Technologies for Multispectral, Hyperspectral, and Ultraspectral Imagery XI*. Bellingham, WA: Proceedings of SPIE.
Canadell, J., Jackson, R.B., Ehleringer, J.R., Mooney, H.A., Sala, O.E., & Schulze, E. -D. (1996). Rooting depth of vegetation types at global scale. *Oecologia*, *108*(4), 583–595.
Castro-Esau, K.L., Sanchez-Azofeifa, G.A., Rivard, B., Wright, S.J., & Quesada, M. (2006). Variability in leaf optical properties of Mesoamerican trees and the potential for species classification. *American Journal of Botany*, *93*(4), 517–530.
Clark, M.L., Roberts, D.A., & Clark, D.B. (2005). Hyperspectral discrimination of tropical rain forest tree species at leaf to crown scales. *Remote Sensing of Environment*, *96*(3–4), 375–398.
Congalton, R.G. (1991). A review of assessing the accuracy of classifications of remotely sensed data. *Remote Sensing of Environment*, *37*(1), 35–46.
da Luz, B.R., & Crowley, J.K. (2007). Spectral reflectance and emissivity features of broad leaf plants: Prospects for remote sensing in the thermal infrared (8.0–14.0 μm). *Remote Sensing of Environment*, *109*(4), 393–405.
Dennison, P.E., & Roberts, D.A. (2003a). The effects of vegetation phenology on endmember selection and species mapping in southern California chaparral. *Remote Sensing of Environment*, *87*(2–3), 295–309.
Dennison, P.E., & Roberts, D.A. (2003b). Endmember selection for Multiple Endmember Spectral Mixture Analysis using endmember average RMSE. *Remote Sensing of Environment*, *87*(2–3), 123–135.
Dubayah, R., & Rich, P. (1995). Topographic solar radiation models for GIS. *International Journal of Geographical Information Systems*, *9*(4), 405–419.
Eliason, S.A., & Allen, E.B. (1997). Exotic grass competition in suppressing native shrubland re-establishment. *Restoration Ecology*, *5*(3), 245–255.
Feret, J. -B., & Asner, G.P. (2011). Spectroscopic classification of tropical forest species using radiative transfer modeling. *Remote Sensing of Environment*, *115*, 2415–2422.
Franke, J., Roberts, D.A., Halligan, K., & Menz, G. (2009). Hierarchical Multiple Endmember Spectral Mixture Analysis (MESMA) of hyperspectral imagery for urban environments. *Remote Sensing of Environment*, *113*, 1712–1723.

Gamon, J.A., Penuelas, J., & Field, C.B. (1992). A narrow-waveband spectral index that tracks diurnal changes in photosynthetic efficiency. *Remote Sensing of Environment*, *41*(1), 35–44.
Gates, D.H. (1980). *Biophysical ecology*. NY: Dover Publications (611 pp.).
Gillespie, A., Rokugawa, S., Matsunaga, T., Cothern, J.S., Hook, S., & Kahle, A.B. (1998). A temperature and emissivity separation algorithm for Advanced Spaceborne Thermal Emission and Reflection Radiometer (ASTER) images. *IEEE Transactions on Geoscience and Remote Sensing*, *36*, 1113–1126.
Goodenough, D.G., Dyk, A., Niemann, O., Pearlman, J.S., Chan, H., Han, T., et al. (2003). Processing Hyperion and ALI for forest classification. *IEEE Transactions on Geoscience and Remote Sensing*, *41*(6), 1321–1331.
Green, R., Eastwood, M., Sarture, C., Chrien, T., Aronsson, M., Chippendale, B., et al. (1998). Imaging spectroscopy and the airborne visible/infrared imaging spectrometer (AVIRIS). *Remote Sensing of Environment*, *65*(3), 227–248.
Gustafson, W.T., Gillespie, A.R., & Yamada, G.J. (2006). Revisions to the ASTER temperature/emissivity separation algorithm. *2nd International Symposium on Recent Advances in Quantitative Remote Sensing* (Torrent (Valencia), Spain).
Hennig, C. (2014). *fpc: Flexible procedures for clustering*. R package version 2.1-7.
Hook, S.J., Myers, J.E.J., Thome, K.J., Fitzgerald, M., & Kahle, A.B. (2001). The MODIS/ASTER airborne simulator (MASTER)—A new instrument for earth science studies. *Remote Sensing of Environment*, *76*(1), 93–102.
Hulley, G.C., Hughes, C.G., & Hook, S.J. (2012). Quantifying uncertainties in land surface temperature and emissivity retrievals from ASTER and MODIS thermal infrared data. *Journal of Geophysical Research-Atmospheres*, *117*.
Kalnay, E., Kanamitsu, M., & Baker, W.E. (1990). Global numerical weather prediction at the National–Meteorological-Center. *Bulletin of the American Meteorological Society*, *71*, 1410–1428.
Kealy, P.S., & Hook, S. (1993). Separating temperature & emissivity in thermal infrared multispectral scanner data: Implication for recovering land surface temperatures. *IEEE Transactions on Geoscience and Remote Sensing*, *31*, 1155–1164.
Kokaly, R.F., & Clark, R.N. (1999). Spectroscopic determination of leaf biochemistry using band-depth analysis of absorption features and stepwise multiple linear regression. *Remote Sensing of Environment*, *67*(3), 267–287.
Kokaly, R.F., Rockwell, B.W., Haire, S.L., & King, T.V.V. (2007). Characterization of post-fire surface cover, soils, and burn-severity at the Cerro Grande Fire, New Mexico, using hyperspectral and multispectral remote sensing. *Remote Sensing of Environment*, *106*, 305–325.
Kummerow, J., Krause, D., & Jow, W. (1977). Root systems of chaparral shrubs. *Oecologia*, *29*(2), 163–177.
Langrebe, D.A. (2000). Information extraction principles and methods for multipspectral and hyperspectral image data. In C.H. Chen (Ed.), *Information processing for remote sensing*. River Edge, N.J.: World Scientific (ch. 1).
Leuzinger, S., & Korner, C. (2007). Tree species diversity affects canopy leaf tempeartures in mature forest. *Agricultural and Forest Meteorology*, *146*, 29–37.
Leuzinger, S., Vogt, R., & Korner, C. (2010). Tree surface temperature in an urban environment. *Agriculture and Forest Meteorology*, *150*, 56–62.
Li, L., Ustin, S.L., & Lay, M. (2005). Application of Multiple Endmember Spectral Mixture Analysis (MESMA) to AVIRIS imagery for coastal salt marsh mapping: a case study in China Camp, CA, USA. *International Journal of Remote Sensing*, *26*(23), 5193–5207.
Martin, M.E., Plourde, L.C., Ollinger, S.V., Smith, M. -L., & McNeil, B.E. (2008). A generalizable method for remote sensing of canopy nitrogen across a wide range of forest ecosystems. *Remote Sensing of Environment*, *112*(9), 3511–3519.
Matsunaga, T. (1994). A temperature-emissivity separation method using an empirical relationship between the mean, the maximum, & the minimum of the thermal infrared emissivity spectrum, in Japanese with English abstract. *Journal of the Remote Sensing Society of Japan*, *14*, 230–241.
McCarthy, H.R., Pataki, D.E., & Jenerette, G.D. (2011). Plant water-use efficiency as a metric of urban ecosystem services. *Ecological Applications*, *21*(8), 3115–3127.
Meentemeyer, R.K., & Moody, A. (2000). Rapid sampling of plant species composition for assessing vegetation patterns in rugged terrain. *Landscape Ecology*, *15*, 697–711.
Moran, M.S., Clarke, T.R., Inoue, Y., & Vida, A. (1994). Estimating crop water deficit using the relation between surface-air temperature and Spectral Vegetation Index. *Remote Sensing of Environment*, *49*, 246–263.
Nascimento, J.M.P., & Bioucas-Dias, J.M. (2005). Vertex component analysis: A fast algorithm to unmix hyperspectral data. *IEEE Transactions on Geoscience and Remote Sensing*, *43*(4), 898–910.
Nemani, R., & Running, S. (1997). Land cover characterization using multitemporal red, near-IR, and thermal-IR data from NOAA/AVHRR. *Ecological Applications*, *7*(1), 79–90.
Ollinger, S.V., Richardson, A.D., Martin, M.E., Hollinger, D.Y., & Frolking, S.E. (2008). Canopy nitrogen, carbon assimilation, and albedo in temperate and boreal forest: Functional relations and potential climate feedbacks. *Proceedings of the National Academy of Sciences*, *105*(49), 19336–19341.
Ollinger, S., & Smith, M.L. (2005). Net primary production and canopy nitrogen in a temperate forest landscape: An analysis using imaging spectroscopy, modeling and field data. *Ecosystems*, *8*(7), 760–778.
Powell, R., Roberts, D.A., Dennison, P., & Hess, L. (2007). Sub-pixel mapping of urban land cover using Multiple Endmember Spectral Mixture Analysis: Manaus, Brazil. *Remote Sensing of Environment*, *106*, 253–267.
R Core Team (2014). *R: A language and environment for statistical computing*. Vienna, Austria: R Foundation for Statistical Computing (URL http://www.R-project.org/).
Richter, R., & Schlaepfer, D. (2002). Geo-atmospheric processing of airborne imaging spectrometry data. Part 2: Atmospheric/topographic correction. *International Journal of Remote Sensing*, *23*, 37–41.
Robakowski, P., Li, Y., & Reich, P.B. (2012). Local ecotype and species range-related adaptation influence of photosynthetic temperature optima in deciduous broadleaved trees. *Plant Ecology*, *213*(1), 113–125.
Roberts, D., Bradley, E., Roth, K., Eckmann, T., & Still, C. (2010). Linking physical geography education and research through the development of an environmental sensing network and project-based learning. *Journal of Geoscience Education*, *58*, 262–274.
Roberts, D. A., Dennison, P.E., Peterson, S., Sweeney, S., & Rechel, J. (2006). Evaluation of AVIRIS and MODIS measures of live fuel moisture and fuel condition in a shrubland ecosystem in Southern California. *Journal of Geophysical Research, Biogeosciences*, *111*, G04S02. http://dx.doi.org/10.1029/2005JG000113 (16 pp.).
Roberts, D., Gardner, M., Church, R., Ustin, S., Scheer, G., & Green, R. (1998). Mapping chaparral in the Santa Monica mountains using multiple endmember spectral mixture models. *Remote Sensing of Environment*, *65*(3), 267–279.
Roberts, Dar A., Quattrochi, D.A., Hulley, G.C., Hook, S.J., & Green, R.O. (2012). Synergies between VSWIR and TIR data for the urban environment: An evaluation of the potential for the Hyperspectral Infrared Imager (HyspIRI) Decadal Survey mission. *Remote Sensing of Environment*, *117*, 83–101.
Roberts, D.A., Smith, M.O., & Adams, J.B. (1993). Green vegetation, nonphotosynthetic vegetation, and soils in AVIRIS data. *Remote Sensing of Environment*, *44*(2–3), 255–269.
Roberts, D.A., Ustin, S.L., Ogunjemiyo, S., Greenberg, J., Dobrowski, S.Z., Chen, J., et al. (2004). Spectral and structural measures of Northwest forest vegetation at leaf to landscape scales. *Ecosystems*, *7*, 545–562.
Roth, K.L. (2014). *Discriminating among plant species and functional types using spectroscopy data: evaluating capabilities within and across ecosystems, across spatial scales and through seasons*. UC Santa Barbara (PhD Dissertation, 255 pp.).
Roth, K.L., Dennison, P.E., & Roberts, D.A. (2012). Comparing endmember selection techniques for accurate mapping of plant species and land cover using imaging spectrometer data. *Remote Sensing of Environment*, *127*, 139–152.
Schaaf, A.N., Dennison, P.E., Fryer, G.K., Roth, K.L., & Roberts, D.A. (2011). Mapping plant functional types at multiple spatial resolutions using imaging spectrometer data. *GIScience and Remote Sensing*, *48*(3), 324–344.
Scherrer, D., Bader, M.K. -F., & Korner, C. (2011). Drought sensitivity ranking of deciduous tree species based on thermal imaging of forest canopies. *Agricultural and Forest Meteorology*, *151*, 1632–1640.
Schimel, D., Pavlick, R., Fisher, J.B., Asner, G.P., Saatchi, S., Townsend, P., et al. (2015). Observing terrestrial ecosystems and the carbon cycle from space. *Global Change Biology* http://onlinelibrary.wiley.com/doi/10.1111/gcb.12822/pdf.
Schlerf, M., & Atzburger, C. (2006). Inversion of a forest reflectance model to estimate structural canopy variables from hyperspectral remote sensing data. *Remote Sensing of Environment*, *100*, 281–294.
Serbin, S.P., Dillaway, D.N., Kruger, E.L., & Townsend, P.A. (2012). Leaf optical properties reflect variation in photosynthetic metabolism and its sensitivity to temperature. *Journal of Experimental Botany*, *63*(1), 489–502.
Serbin, S.P., Singh, A., McNeil, B.E., Kingdon, C.C., & Townsend, P.A. (2014). Spectroscopic determination of leaf morphological and biochemical traits for northern temperate boreal tree species. *Ecological Applications*, *24*(7), 1651–1669.
Sims, D.A., & Gamon, J.A. (2003). Estimation of vegetation water content and photosynthetic tissue area from spectral reflectance: A comparison of indices based on liquid water and chlorophyll absorption features. *Remote Sensing of Environment*, *84*(4), 526–537.
Somers, B., & Asner, G.P. (2012). Hyperspectral time series analysis of native and invasive species in Hawaiian rainforests. *Remote Sensing*, *4*, 2510–2529.
Somers, B., & Asner, G.P. (2013). Invasive species mapping in Hawaiian rainforests using multi-temporal hyperion spaceborne imaging spectrometry. *IEEE Journal on Selected Topics in Applied Earth Observations and Remote Sensing*, *6*(2), 351–359.
Sparks, J.P., & Black, R.A. (1999). Regulation of water loss in populations of *Populus trichocarpa*: The role of stomatal control in preventing xylem cavitation. *Tree Physiology*, *19*, 453–459.
Tonooka, H. (2005). Accurate atmospheric correction of ASTER thermal infrared imagery using the WVS method. *IEEE Transactions on Geoscience and Remote Sensing*, *43*, 2778–2792.
Townsend, P.A., Foster, J.R., Chastain, R.A., & Currie, W.S. (2003). Application of imaging spectroscopy to mapping canopy nitrogen in the forests of the Central Appalachian Mountains using Hyperion and AVIRIS. *IEEE Transactions on Geoscience and Remote Sensing*, *41*(6), 1347–1354.
Ullah, S., Schlerf, M., Skidmore, A.K., & Hecker, C. (2012). Identifying plant species using mid-wave infrared (2.5–6 μm) and thermal infrared (8–14 μm) emissivity spectra. *Remote Sensing of Environment*, *118*, 95–102.
Ustin, S.L., Gitelson, A.A., Jacquemoud, S., Schaepman, M., Asner, G., Gamon, J.A., et al. (2009). Retrieval of foliar information about plant pigment systems from high resolution spectroscopy. *Remote Sensing of Environment*, *113*, 567–577.
Ustin, S.L., Roberts, D.A., Pinzon, J., Jacquemoud, S., Gardner, M., Scheer, G., et al. (1998). Estimating canopy water content of chaparral shrubs using optical methods. *Remote Sensing of Environment*, *65*(3), 280–291.
Youngentob, K.N., Roberts, D.A., Held, A.A., Dennison, P.E., Jia, X., & Lindenmayer, D.B. (2011). Mapping two Eucalyptus subgenera using Multiple Endmember Spectral Mixture Analysis and continuum-removed imaging spectrometry data. *Remote Sensing of Environment*, *115*(5), 1115–1128.